Monthly Notices of the ROYAL ASTRONOMICAL SOCIETY

MNRAS **491,** 1127–1145 (2020) doi:10.1093/mnras/stz2954
Advance Access publication 2019 October 21

Deep GMRT 610 MHz observations of the ELAIS N1 field: catalogue and source counts

E. F. Ocran [1,2★] A. R. Taylor, [1,2,3★] M. Vaccari [2,3,4★] C. H. Ishwara-Chandra [2,5] and I. Prandoni [4]

[1] *Department of Astronomy, University of Cape Town, Private Bag X3, Rondebosch 7701, South Africa*
[2] *Inter-University Institute for Data Intensive Astronomy, Cape Town, Private Bag X3, Rondebosch, 7701, South Africa*
[3] *Department of Physics and Astronomy, University of the Western Cape, Private Bag X17, Bellville 7535, South Africa*
[4] *INAF – Istituto di Radioastronomia, via Gobetti 101, I-40129 Bologna, Italy*
[5] *National Centre for Radio Astrophysics, Tata Institute of Fundamental Research, Pune 411007, India*

Accepted 2019 October 17. Received 2019 October 17; in original form 2019 June 23

ABSTRACT

This is the first of a series of papers based on sensitive 610 MHz observations of the ELAIS N1 field, using the Giant Metrewave Radio Telescope. We describe the observations, processing and source catalogue extraction from a deep image with area of 1.86 deg^2 and minimum noise of $\sim$7.1 μJy beam^{-1}. We compile a catalogue of 4290 sources with flux densities in the range of 28.9 μJy– 0.503 Jy and derive the Euclidean-normalized differential source counts for sources with flux densities brighter than 35.5 μJy. Our counts show a flattening at 610 MHz flux densities below 1 mJy. Below the break the counts are higher than previous observations at this frequency, but generally consistent with recent models of the low-frequency source population. The radio catalogue is cross-matched against multiwavelength data leading to identifications for 92 per cent and reliable redshifts for 72 per cent of our sample, with 19 per cent of the redshifts based on spectroscopy. For the sources with redshifts, we use radio and X-ray luminosity, optical spectroscopy and mid-infrared colours to search for evidence of the presence of an active galactic nucleus (AGN). We compare our identifications to predictions of the flux density distributions of star-forming galaxies (SFGs) and AGN, and find a good agreement assuming the majority of the sources without redshifts are SFGs. We derive spectral index distributions for a sub-sample. The majority of the sources are steep spectra, with a median spectral index that steepens with frequency: $\alpha_{325}^{610} = -0.80 \pm 0.29$, $\alpha_{1400}^{610} = -0.83 \pm 0.31$, and $\alpha_{5000}^{610} = -1.12 \pm 0.15$.

Key words: galaxies: active – infrared: galaxies – radio continuum: galaxies.

1 INTRODUCTION

The study of the faint radio continuum universe and of its properties has recently become a very active field of research not only because of the planned transformational capabilities of the Square Kilometre Array (Braun et al. 2015) on this field but also because of the major steps being taken and planned with SKA pathfinders and precursors. Deep radio observations of the extragalactic sky are a powerful means to probe the properties of diverse source populations over a variety of environments to high redshift (Condon 1984; Becker, White & Helfand 1995; Gruppioni et al. 1999). Radio emission is important for galaxy population studies, as the synchrotron emission is a clear indicator of activity for both star-forming galaxies (SFGs) and active galactic nuclei (AGNs). Moreover, radio emission is not affected by dust obscuration, hence can probe astrophysical processes to large distances.

At faint radio flux densities, SFGs dominate. These are very different from the radio sources seen in the bright radio sky (Windhorst et al. 2011; Padovani 2016a), which are dominated by active galaxies. Counts of radio galaxies versus flux density provide useful information, as the source count shape is directly related to the evolutionary properties of the galaxies (Prandoni et al. 2001; de Zotti et al. 2010; Padovani et al. 2011, 2015). Radio source counts represent the most immediate observational constraint to evolutionary models of radio sources (Prandoni et al. (2001). The now well-established flattening of the counts below 1 mJy is interpreted as the signature of the rise of SFGs (Rawlings & Jarvis 2004; Seymour et al. 2008; Padovani et al. 2009).

★ E-mail: ocran62@gmail.com (EFO); russ@ast.uct.ac.za (ART); mattia.vaccari@gmail.com (MV)

Surveys at low frequencies (e.g. Garn et al. 2008; Sirothia et al. 2009; Williams et al. 2016) are an important complement to higher frequency observations. Low-frequency observations are powerful at detecting ultra-steep spectrum sources, which are often galaxies at high redshifts (e.g. Best et al. 1998, 2003; Miley & De Breuck 2008). Combining low- and high-frequency radio observations allows studies of the radio continuum spectra (e.g. Whittam et al. 2017; Mahony et al. 2016), providing a more precise characterization of the source properties (Riseley et al. 2016). Radio spectral indices can be used to identify GHz-peaked sources (GPS; Athreya & Kapahi 1998; O'Dea 1998; Snellen, Schilizzi & van Langevelde 2000), ultra-steep spectrum sources (USS; Roettgering et al. 1994; Jarvis et al. 2001), and core-dominated radio-quiet AGN (Blundell & Kuncic 2007).

SFGs are observed to have a mean spectral index between −0.8 and −0.7 at 1.4 GHz ($S(\nu) \propto \nu^{\alpha}$), with a relatively small dispersion of ±0.24 (Condon 1992). Studies combining 610 MHz and 1.4 GHz data have found evidence for flatter spectral indices (Bondi et al. 2007; Garn et al. 2008) and larger dispersions at sub-mJy radio flux densities (Magliocchetti, Andreani & Zwaan 2008), suggesting that core-dominated radio-quiet AGNs are playing a key role in the sub-mJy radio population. Ibar et al. (2009) reported statistical analyses showing no clear evolution for the median spectral index, α_{1400}^{610}, as a function of flux density based on observations of the Lockman Hole using the Giant Metrewave Radio Telescope (GMRT). Their study found α_{1400}^{610} to be −0.6 to −0.7. They also analyse the spectral indices based independently on GMRT- and VLA-selected samples and found that a 610 MHz-selected catalogue naturally tends to prefer the detection of steep-spectrum sources while selection at 1.4 GHz favours flatter spectra.

The European Large Area *ISO* Survey (ELAIS) N1 field has been observed at multiple radio frequencies. Sirothia et al. (2009) observed it at 325 MHz using the GMRT, with the objective of identifying AGNs and starburst galaxies and examining their evolution with cosmic epoch. Grant et al. (2010) observed 15 deg^2 with the Dominion Radio Astrophysical Observatory synthesis telescope at 1420 MHz to a minimum rms of 55 μJy beam^{-1} in Stokes I and 45 μJy beam^{-1} in polarization. Banfield et al. (2011) observed 10 deg^2 at 1.4 GHz with the JVLA in B configuration to a minimum rms of 87 μJy beam^{-1} in total intensity. Taylor et al. (2014) observed a smaller region (0.13 deg^2) at 5 GHz with the JVLA in B and C configuration to a minimum rms of 1.05 μJy beam^{-1}.

In this paper, we present deep GMRT observations at 610 MHz of the ELAIS N1 field (EN1) covering 1.86 deg^2. The EN1 field is a large northern field that has been targeted by surveys spanning the entire electromagnetic spectrum. Further building on the extensive radio coverage of ELAIS N1 and wealth of multiwavelength observations that provides valuable insights into galaxy formation and evolution. In this work, we achieve a minimum noise of 7.1 μJy beam^{-1} and an angular resolution of 6 arcse × 6 arcsec.

The remainder of this paper is divided as follows: we first introduce the observations and data processing in Section 2. In Section 3, we present the 610 MHz source counts analysis. Section 4 provides the multiwavelength cross-identifications and the nature of the source population. The multifrequency spectral analysis of the sample is presented in Section 5. In this paper, we assume a flat cold dark matter (ΛCDM) cosmology with $\Omega_{\Lambda} = 0.7$, $\Omega_{\rm m} = 0.3$, and $H_{\rm o} = 70\,{\rm km\,s^{-1}\,Mpc^{-1}}$.

2 OBSERVATIONS AND DATA PROCESSING

2.1 Radio data

The ELAIS N1 field was originally chosen for deep extragalactic observations with the Infrared Space Observatory (*ISO*) due to its low-infrared background (Rowan-Robinson et al. 2004; Vaccari et al. 2005). Since then, it has become one of the best-studied 1–10 deg^2 extragalactic fields. GMRT observations of the ELAIS N1 field were obtained during several observing runs from 2011 to 2013. The observations were carried out for seven positions arranged in a hexagonal pattern centred on $\alpha = 16^{\rm h}10^{\rm m}30^{\rm s}$, $\delta = 54^{\circ}35'00''$ (see Ocran et al. 2017). In this paper, we present a deeper radio image, an improved radio data reduction and multiwavelength analysis of the ELAIS N1 610 MHz Deep Survey first described by Ocran et al. (2017).

The survey consists of seven closely spaced GMRT pointings, with on source integration time of ∼18 h per pointing. The pipeline was modified to restrict the flags, which resulted in slightly less data being flagged. The shallower pointings were added at the edges where the deep and shallow pointing had rms within a factor of 2. The weights used in the mosaic follows the same procedure as in Intema et al. (2017), Section 3.3. The weight is the inverse square of the local background rms noise (the inverse variance). The resolutions before mosaic, for each pointing were in the range of 4.5–6 arcsec. To reduce the noise around the edges of the mosaic image we included data from a set of pointings with 3 h of observation each that are part of a wider but shallower study of ELAIS N1 (Ishwara-Chandra et al., in preparation).

The data was analysed using CASA (COMMON ASTRONOMY SOFTWARE APPLICATIONS) using standard procedures. The flux density scale was set using the primary calibrators 3C 286 and 3C 48, which were observed both at the start and at the end of each observing session. A phase calibrator was observed for 5 min every 30 min of target observations for phase and gain calibrations. After initial flagging using `flagdata`, delay, bandpass, and gain calibration was carried out. Post-calibration, the data were flagged again and re-calibrated. Channel averaging was done with post-averaging channel width of 0.78 MHz in order to keep the bandwidth smearing negligible. Split files from each pointing from different observing runs were combined using `concat` before imaging. We used `tclean` for imaging. Four rounds of phase-only self-cal and then five rounds of amplitude and phase self-cal was carried out on each pointing. The rms noise on the individual images were ∼15 μJy beam^{-1} before mosaicing. The primary beam correction and mosaic was carried out in AIPS using the python script *make mosaic* (Intema, private communication) using a circular restoring beam of 6 arcsec.

An image of the mosaic is shown in Fig. 1. There are a small number of bright classical radio galaxies with double-lobed and jet morphologies; however, most of the sources are compact as typically found in faint (sub-) mJy radio fluxes. Fig. 2 shows an image of the rms map created by PYBDSF, and Fig. 3 shows the distribution of pixel amplitudes in the rms image. The minimum rms noise in the central region of the image is 7.1 μJy beam^{-1}. The median noise in the mosaic is 19.5 μJy beam^{-1}. The higher noise values arise primarily due to enhanced rms in small regions around very bright sources and from the lower mosaic weights at the edge of the mosaic.

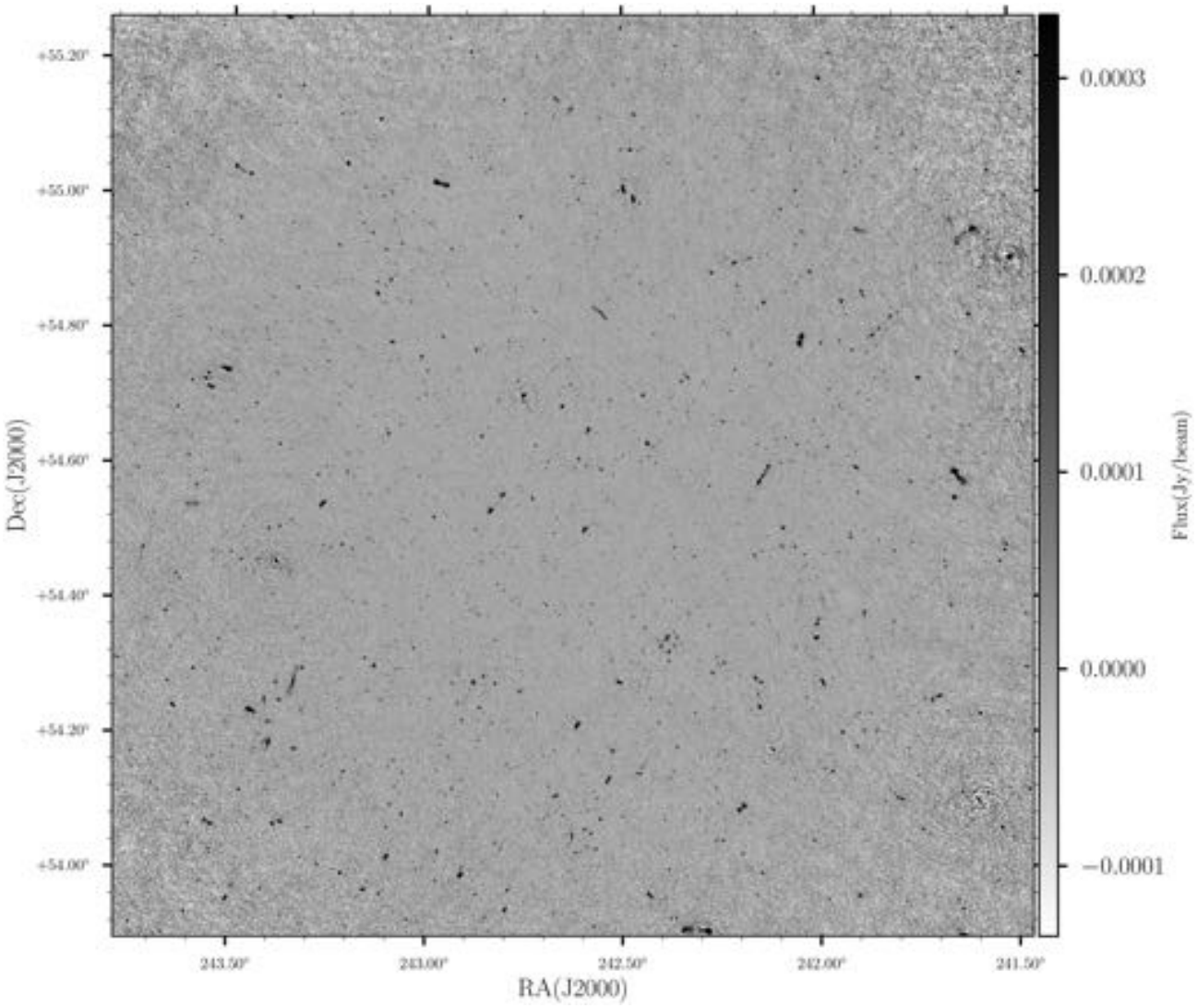

Figure 1. Image of the ELAIS N1 GMRT 610 MHz mosaic centred at $\alpha = 16^{\rm h}10^{\rm m}30^{\rm s}$, $\delta = 54^{\circ}\ 35\ 00''$ (J2000). This image is 47 arcmin on each side. The restoring beam is 6 arcsec circular and the rms in the central region is ~ 7.1 μJy beam^{-1}. The grey-scale brightness stretch ranges between −0.1 and 0.3 mJy beam^{-1}.

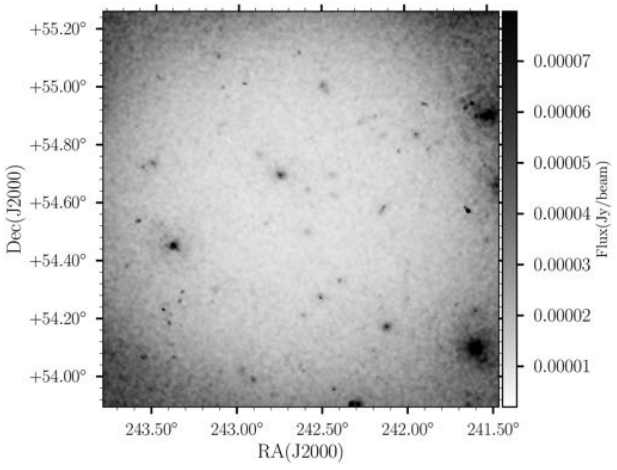

Figure 2. Grey-scale image showing the local rms noise of the final mosaicked GMRT image, derived using PyBDSF (see Section 2.2). The grey-scale brightness stretch ranges between 0.01 and 0.07 mJy beam^{-1}.

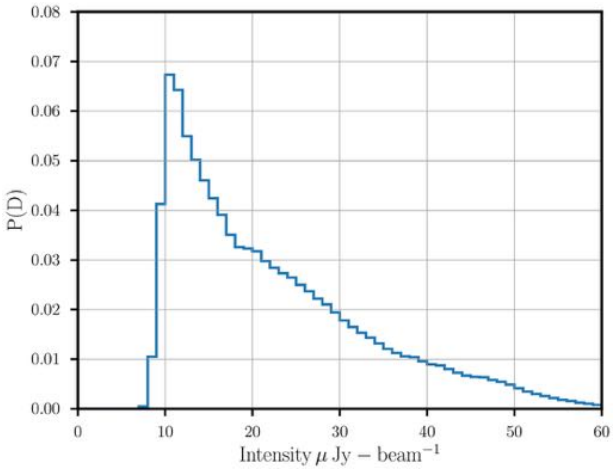

Figure 3. The distribution of the 610 MHz rms for the GMRT sample. The mean and median rms are 22.70 and 19.50 μJy, respectively.

2.2 Source finding and cataloguing

The catalogue of radio sources was extracted using the PyBDSF source finder (Mohan & Rafferty 2015). The rms map was determined with a sliding box `rms_box`= (80, 10) pixels (i.e. a box size of 80 pixels every 10 pixels), with a smaller box `rms_box_bright` = (40, 5) pixels in the regions around bright sources to account for the increase in local rms as a result of calibration artefacts. Fig. 2 illustrates the variation in rms noise determined across the entire mosaic image.

PyBDSF extracts sources by first identifying islands of contiguous emission above a given threshold `thresh_isl`= 3σ, around pixels brighter than a given flux `thresh_pix`= 5σ. Then it decomposes the islands into Gaussian components. It then combines significantly overlapping Gaussians into sources and determines the flux densities, shapes, and positions of sources (Intema et al. 2011). We used the `group_tol` parameter with a value of 10.0 to allow more Gaussians to be grouped together and larger sources to be formed. Sources are classified as '*S*' for single sources and '*M*' for multiple Gaussian sources. The total number of sources detected by PyBDSF in the image is 6605 comprising of 7919 Gaussian components of which 5682 were single-component sources.

The catalogue consists of 4303 radio sources with signal-to-noise cut (SNR $= \frac{S_p}{\mathrm{rms}}$) above the 5σ threshold and flux threshold cut $\geq 0.1 \times \mathrm{RMS_{median}}$. 128 of the sources included in the catalogue flagged as having poor Gaussian fits. In this case the integrated flux density is the total flux measured in the island instead of that defined by the Gaussian fit.

2.3 Multiple component sources

In order to generate a final source catalogue, we need to identify multicomponent sources that have not been recognized as such by `PyBDSF`, and therefore appear as a distinct radio source in the catalogue. This can happen when there is no significant radio emission between two radio lobes, or the local rms noise is overestimated because of large-scale faint radio emission (see Smolčić et al. 2017), which affects the ability of PyBDSF to properly detect the source.

Fig. 4 shows examples of such sources (typically radio galaxies or resolved star-forming discs). For the identification of these objects, we make use of the Spitzer Extragalactic Representative Volume Survey (SERVS; Mauduit et al. 2012) that imaged 18 deg^2 using the IRAC1 3.6 μm and IRAC2 4.5 μm bands. SERVS overlaps with several other surveys from the optical, near- through far-infrared, sub-millimetre and radio. We overlaid radio contours on IRAC1 3.6 μm postage stamps. If we clearly identify an SERVS counterpart, we take the SERVS position to be the position of the radio source. Otherwise the radio source positions were determined by averaging the peak positions of the radio emission. The total and peak flux densities were estimated by summing the flux density inside regions guided by contours. Fig. 5 shows examples of SERVS+radio cut-outs of extended or otherwise complex sources in the catalogue (i.e. more examples of these sources are shown in Fig. A1).

Following the above process, we produced a curated catalogue of 4290 sources that we used for our science analyses.

3 SOURCE COUNTS

We derived number counts in the EN1 using the curated catalogue shown in Table 2. The radio number counts require no additional data but nevertheless provide very useful information, as their shape is tightly related to the evolutionary properties of the sources and also to the geometry of the Universe Padovani (2016b). The differential number counts, dN/dS, were calculated using the observed number of sources per bin of flux density, N, corrected for the estimated number of false detections N_f, divided by the bin width (ΔS in Jy) and multiplied by the weight, w (which incorporates the efficiency, resolution bias C_R, and Eddington bias $\mathrm{C_{Edd}}$)

$$\frac{\mathrm{d}N}{\mathrm{d}S} = \frac{N - N_\mathrm{f}}{\Delta S} \times w. \quad (1)$$

In this section, we discuss how we derive our source counts alongside our treatment of efficiency, resolution bias, and Eddington bias.

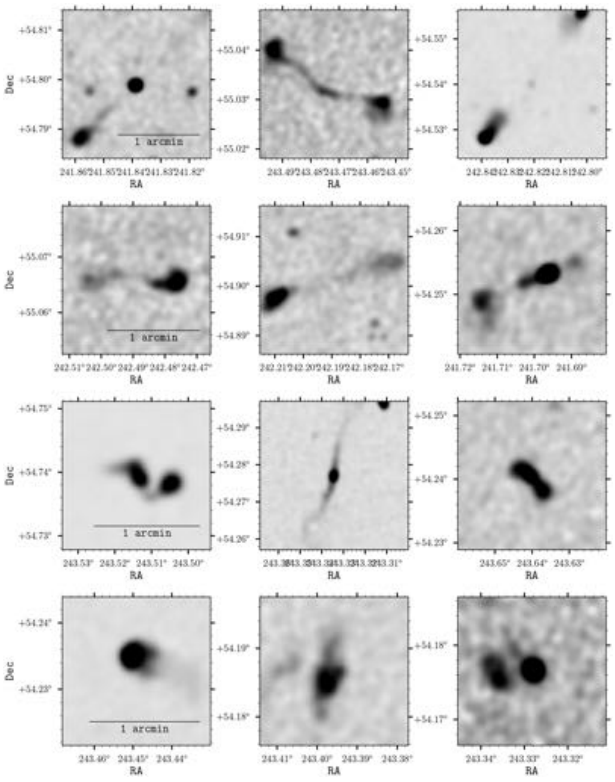

Figure 4. Postage stamps from the GMRT 610 MHz continuum mosaic image showing some extended radio sources.

3.1 Source sizes

The flux density ratio may be used to discriminate between point-like and extended sources (see Prandoni et al. 2001, 2006). The ratio of the integrated to peak flux densities is shown as a function of signal-to-noise ratio in Fig. 6, with sources classified as point-like and extended shown separately. To select the resolved components, we determined the lower envelope of the points in Fig. 6, by fitting a functional form that can be characterized by equation (2). Almost all of the points with $S_i/S_p < 1$ lie above the curve. Reflecting this curve above the $S_i/S_p = 1$ line (upper envelope in Fig. 6) gives a list of all the sources that lie above the upper envelope and can be considered to be resolved. This analysis shows that about 29 per cent of the sources (1260/4290) are considered to be resolved:

$$\frac{S_i}{S_p} = 1.0 \pm \frac{3}{\mathrm{SNR}}, \quad (2)$$

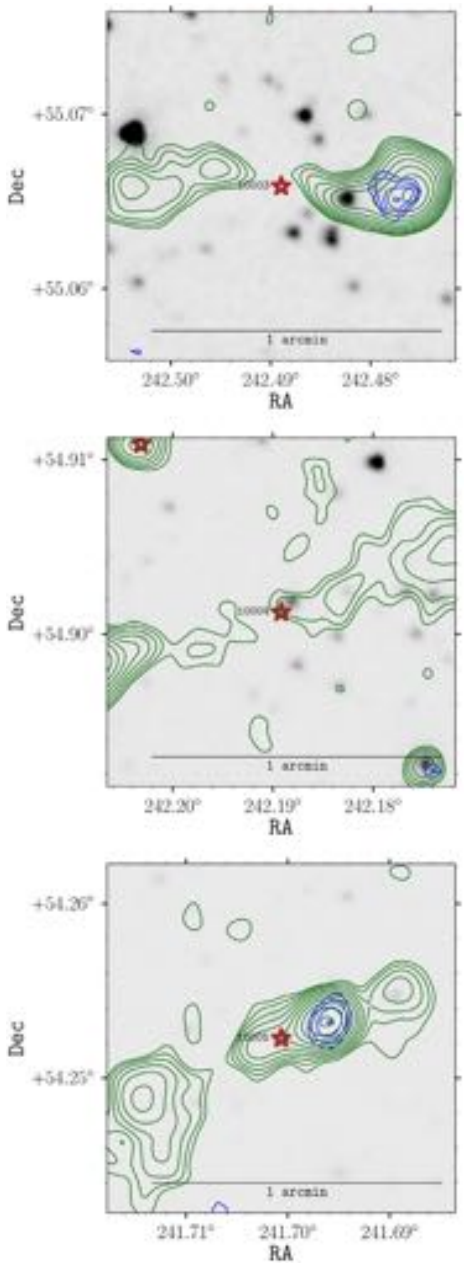

Figure 5. Postage stamps showing examples of multiple component sources in the GMRT 610 MHz catalogue. The grey-scale shows IRAC band 1 and IRAC band 2 images, respectively. The red stars show the central position of the GMRT source. The green contours represents the GMRT 610 MHz, whereas the blue contours represent VLA FIRST. The contours levels are 1, 2, 3, 4, 5, and 6σ.

where SNR $= \frac{S_p}{\mathrm{rms}}$. Sources below this locus are considered to be unresolved. These resolved and unresolved components were flagged in the catalogue. We use the peak flux density as recovered by PyBDSF in place of the integrated flux density for unresolved sources when deriving the differential source counts.

3.2 Reliability

The reliability of a source catalogue is defined as the probability that all detected sources in the survey area above a certain brightness

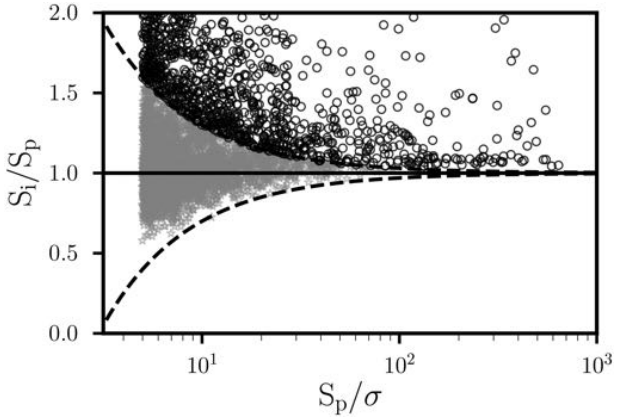

Figure 6. Ratio of the integrated flux density to peak flux density as a function of signal-to-noise ratio (S_p/σ). Sources that are classified as unresolved (grey stars) and resolved (open black circles) during the source-fitting procedure. The solid line is at $S_i/S_p = 1$.

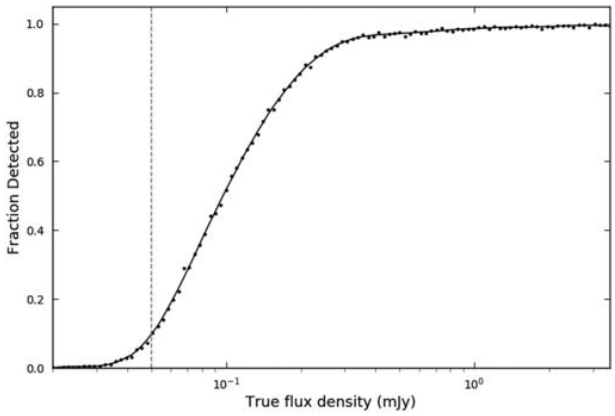

Figure 7. The fraction of simulated sources detected as a function of flux density illustrated by the blue solid curve. The solid line is a piece-wise polynomial spline interpolation of the data. The vertical dashed line shows the approximate 5σ detection level of 50 μJy beam^{-1}.

detect limit are real sources and are not detections of artefacts or noise peaks (Williams et al. 2016; Whittam et al. 2017).

We investigate the effect these may have on the false detection rate by running the PyBDSF algorithm with the same parameters we use to compile the source catalogue on an inverted image in exactly the same way as described in Section 2.2. The source finding algorithm only detects positive peaks; therefore by inverting the image and running PyBDSF on the inverted map, any detections result from noise on the map Whittam et al. (2017). We detected 192 sources in the inverted image (compared to 6605 in the real image), giving a false detection rate of 2.5 per cent, which indicates that the noise in the image is not entirely Gaussian. We corrected for false sources the source counts by subtracting the negative sources in each flux bin before calculating the counts.

3.3 Resolution bias

The underestimation of source counts in a given flux density bin due to a resolved component having a lower peak flux density than

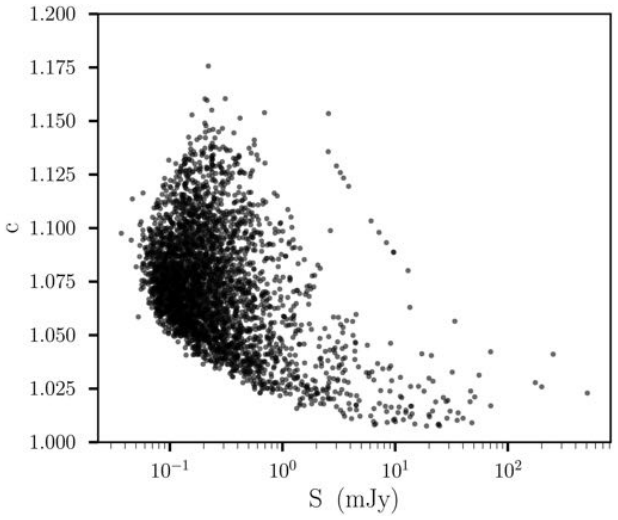

Figure 8. The resolution bias correction factor $c_R = 1/[1 - h(> \max)]$ as a function of flux density.

an unresolved component with equivalent integrated flux density is defined as resolution bias (e.g. see Kellermann & Wall 1987; Prandoni et al. 2001; Williams et al. 2016). We calculate the approximate maximum size θ_{max} a source could have for a given integrated flux density before it drops below the peak flux detection threshold. Using the relation below:

$$\frac{S_{int}}{S_{peak}} = \frac{\theta_{maj}\theta_{min}}{b_{maj}b_{min}}, \tag{3}$$

where b_{min} and b_{maj} are the synthesized beam axes, and θ_{min} and θ_{maj} are the deconvolved source axes, we estimate the maximum size a source of a given integrated flux density can have before falling below the peak flux detection threshold:

$$\theta_{max} = \left[(b_{maj}b_{min})\frac{S_{int}}{5\sigma}\right]^{0.5}. \tag{4}$$

Combining the upper envelope for resolved sources defined in equation (2) (see Section 3.1) with equation (3) gives

$$\theta_{min} = \left[(b_{maj}b_{min})\left(1 + \frac{3}{SNR}\right)\right]^{0.5}, \tag{5}$$

where θ_{min} is the minimum angular size a source can have before it can be considered to be resolved as a function of its SNR (see Heywood et al. 2016). We estimate the fraction of sources with deconvolved angular sizes larger than this θ_{max} limit, using the assumed true angular size distribution proposed by Windhorst, Mathis & Neuschaefer (1990):

$$h(> \theta) = \exp\left[-\ln 2\left(\frac{\theta_{lim}}{\theta_{med}}\right)^{0.62}\right], \tag{6}$$

where $\theta_{lim} = \max(\theta_{min}, \theta_{max})$ and $\theta_{med} = 2\,S^{0.3}_{1.4GHz}$ (S is the flux at 1.4 GHz density in mJy, we have scaled the 1.4 GHz flux densities to 610 MHz with a spectral index of −0.8).

The resolution bias correction factor c_R for the counts is then given by

$$C_R = \frac{1}{1 - h(> \theta_{lim})}. \tag{7}$$

The correction factors calculated using the median size distributions is plotted as a function of flux density in Fig. 8.

3.4 Completeness and Eddington bias

Eddington (1913) showed that there was a significant bias in the measured number counts of stars even when the errors on the flux densities of the stars have the usual Gaussian distribution. This causes the apparent steepening of the observed source count by the intensity-dependent overestimation of intensities, due to either system noise or confusion noise or both (Zwart et al. 2015). This effect is more significant near the detection limit of a survey and could cause the number of observed sources to be slightly too high in the fainter bins. To quantify the effect that Eddington bias has on source counts, previous work at higher frequency have semi-empirical methods. For example, Moss et al. (2007) used the best-fitting population model of the source count extrapolated to 60 μJy as a prediction of the source counts below the detection limit. They subsequently derive counts from this population and use the difference between the recovered population and input model to quantify the Eddington bias.

To correct for both Eddington bias and the detection efficiency as a function of flux density, we followed the approach outlined in Ishwara-Chandra et al., in preparation, which uses simulations to take into account the variation of the noise background of the mosaic image. The observed differential source counts can be related to the true source counts as

$$\frac{\mathrm{d}}{N_o}(\mathrm{s}')\mathrm{d}s' = \int_0^\infty \frac{\mathrm{d}N_t(s)}{\mathrm{d}s\,\epsilon(s)\,\mathrm{p}(s, s')\,\mathrm{d}s}. \tag{8}$$

Here, $\mathrm{d}N_o(s')/\mathrm{d}s'$ is the observed count at observed flux densities s', and $\mathrm{d}N_t(s)/\mathrm{d}s$ is the true source count at the true flux s. The function $p(s, s')$ is the normalized probability density function that a source at observed flux s' is due to a source with true flux density s, and $\epsilon(s)$ is the probability that a source with true flux density, s, will result in a detection – the completeness of the source catalogue versus true flux density. We measured both function by inserting 3000 artificial point sources at a given true flux density at random positions into the residual map with the original sources removed. These sources populate the image with the same background noise and rms properties as the original source finding. The image was then searched for sources using the same parameters as for the real source list. Fig. 7 shows the result for $\epsilon(s)$. The field-of-view effect dominates the curve in Fig. 7, since the analysis is incorporating the varying sensitivity limit across the field of view due to the GMRT primary beam. The effect of Eddington bias is clearly seen in the fact that sources with true flux well below the detection threshold have significant probability to produce detections. The combined completeness and Eddington bias correction is derived by iteratively inverting equation (8) to derive the correction factor that relates the true count to the observed count (see Ishwara-Chandra et al., in preparation, for details).

3.5 The 610 MHz source counts

To compute the 610 MHz source counts, we used the integrated flux density if a source is classified as extended using the criteria described in Section 3.1. If a source is point like, we instead use the peak-flux density since this provides a better measure of the flux density of unresolved sources (Sirothia et al. 2009; Whittam et al. 2017). We compute the weight that takes into account the efficiency ϵ(s), resolution bias C_R, and Eddington bias C_{Edd}, given by the equation below:

$$w = \frac{1}{\epsilon(s)} \times C_R \times C_{Edd}.$$

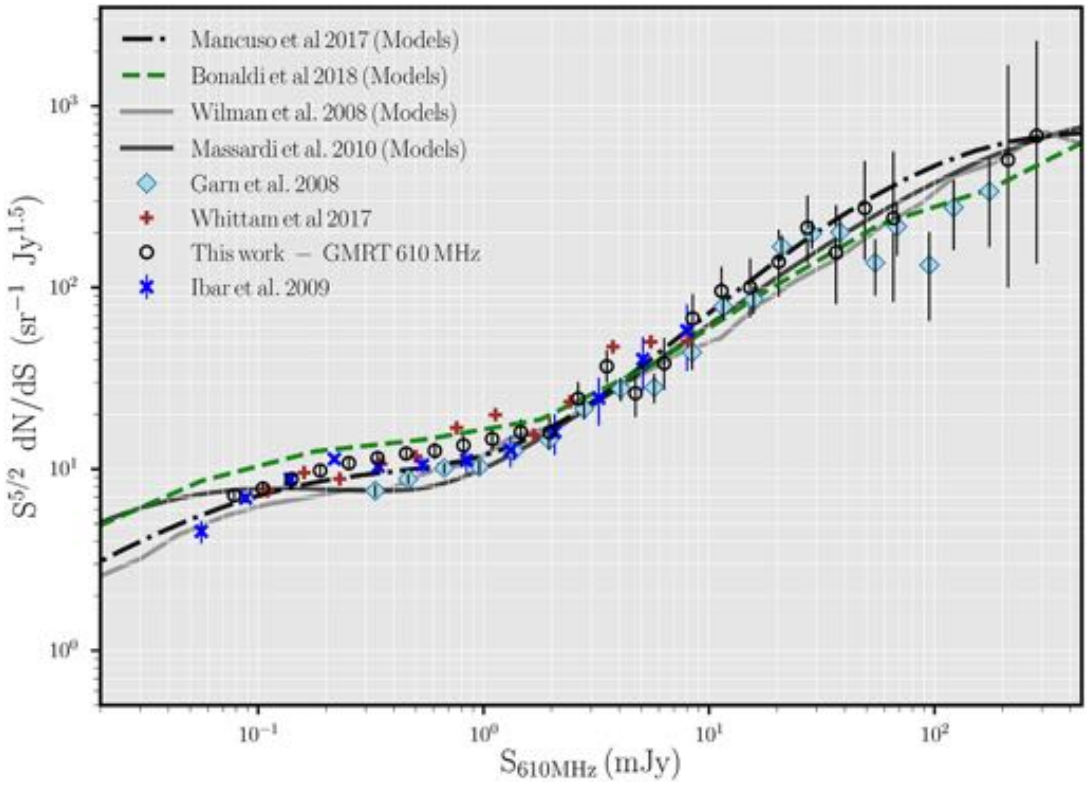

Figure 9. Normalized 610 MHz differential source counts as derived from the catalogue discussed in this work (black points). Vertical bars represent Poissonian errors on the normalized counts. We compare with results from previous observations at 610 MHz including Garn et al. (2008, filled blue diamonds); Ibar et al. (2009, blue stars); and Whittam et al. (2017, brown pluses). We also compare against various models at 610 MHz including Wilman et al. (2008, solid grey curve); Massardi et al. (2010, solid black curve); Mancuso et al. (2017, dot–dashed black curve); and Bonaldi et al. (2019, dashed green curve).

Fig. 9 illustrates the Euclidean-normalized differential source counts as derived from the catalogue discussed in this work (filled black points). The source counts are tabulated in Table 1. Uncertainties on the final normalized source counts are propagated from the errors on the reliability and resolution bias correction factors and the Poisson errors using the prescription of Gehrels (1986) on the raw counts per bin. We do not add uncertainties associated with the Eddington bias correction due to the computational expense of running the full required simulation. The bin sizes are in linear space and statistically independent. Each bin's upper limit is 1.34 times the lower limit. We note that for bins 75.264–100.854, 100.854–135.145, and 135.145–181.094, there are no sources in these bins hence the count is zero.

Many studies have observed a flattening in the source counts below 1 mJy at 1.4 GHz (Condon 1984; Fomalont et al. 1984; Windhorst 1984). This flattening has been later observed also at other frequencies, including 610 MHz (Garn et al. 2008; Ibar et al. 2010; Whittam et al. 2017). This work confirms this flattening ∼1 mJy down to at least 100 μJy (see Fig. 9). Below 100 μJy our counts are probably less reliable, and we cannot entirely believe in the re-steepening we see. Our counts seems to be in better agreement with the later, but we caveat that existing radio source count models are better constrained at higher frequency (1.4 GHz) and their extrapolation to much lower frequency heavily relies on the assumptions on the spectral index source distribution.

In this work, we extend the number counts down to very faint 610 MHz flux densities whilst maintaining good agreement with simulations of previous studies at this frequency. Simulated counts by Massardi et al. (2010) are also shown in solid black curve in Fig. 9. Mancuso et al. (2017) investigated the astrophysics of radio-emitting SFGs and AGNs and explained their statistical properties in the radio band including number counts. The dotted–dashed black curve in Fig. 9 shows the Mancuso et al. (2017) models we compare to our work. The dashed green curve in Fig. 9 shows the simulated 610 MHz counts from the Tiered Radio Extragalactic Continuum Simulation (T-RECS) by Bonaldi et al. (2019). This new simulation of the radio sky in continuum models two main populations of radio galaxies: AGNs and SFGs, and corresponding sub-populations, over the 150 MHz–20 GHz range.

4 MULTIWAVELENGTH CROSS-IDENTIFICATION

4.1 Cross-matching

One advantage of the ELAIS N1 field is the wealth of multiwavelength data publicly available in the field to study the properties of radio sources. Most of this public data have been homogeneized as part of the SERVS Data Fusion project[1] (Vaccari et al. 2010; Vaccari 2015) and of The Herschel Extragalactic Legacy Project (Vaccari 2015).[2]

To determine their multiwavelength counterparts, we first matched GMRT radio sources against the Spitzer Extragalactic Representative Volume Survey SERVS DR2 (Mauduit et al. 2012;

[1] http://www.mattiavaccari.net/df
[2] https://herschel.sussex.ac.uk

Table 1. 610 MHz radio source counts within the EN1 1.864 deg^2 field, normalized to Euclidean geometry. We chose fixed (in linear space) bin sizes and non-overlapping (statistically independent) bins.

S_{range} (mJy) (1)	S_{width} (mJy) (2)	S_{mid} (mJy) (3)	Area (deg^2) (4)	$\mathcal{C}_{Edd}$ (5)	N (6)	Count (Jy$^{1.5}$ sr^{-1}) (7)
0.067–0.090	0.023	0.078	0.667	3.041	559	$7.165^{+0.552}_{-0.538}$
0.090–0.120	0.030	0.105	1.009	1.981	612	$7.802^{+0.583}_{-0.571}$
0.120–0.161	0.041	0.141	1.313	1.326	670	$8.802^{+0.585}_{-0.572}$
0.161–0.216	0.055	0.189	1.546	1.148	566	$9.814^{+0.613}_{-0.596}$
0.216–0.289	0.073	0.253	1.705	1.032	447	$10.787^{+0.713}_{-0.686}$
0.289–0.388	0.098	0.339	1.783	1.016	316	$11.490^{+0.832}_{-0.796}$
0.388–0.520	0.132	0.454	1.807	0.926	234	$12.173^{+0.961}_{-0.909}$
0.520–0.696	0.177	0.608	1.818	0.987	150	$12.612^{+1.234}_{-1.141}$
0.696–0.933	0.237	0.815	1.831	1.105	90	$13.511^{+1.576}_{-1.426}$
0.933–1.251	0.317	1.092	1.840	1.000	68	$14.653^{+2.004}_{-1.767}$
1.251–1.676	0.425	1.463	1.846	1.000	49	$15.969^{+2.607}_{-2.281}$
1.676–2.246	0.570	1.961	1.848	1.000	32	$15.906^{+3.330}_{-2.784}$
2.246–3.009	0.764	2.627	1.854	1.000	31	$24.397^{+5.448}_{-4.582}$
3.009–4.032	1.023	3.521	1.859	1.000	31	$36.792^{+7.833}_{-6.539}$
4.032–5.403	1.371	4.718	1.864	1.000	16	$26.159^{+8.338}_{-6.539}$
5.403–7.240	1.837	6.322	1.864	1.000	13	$38.250^{+13.829}_{-10.592}$
7.240–9.702	2.462	8.471	1.864	1.000	14	$67.653^{+23.195}_{-17.879}$
9.702–13.001	3.299	11.351	1.864	1.000	14	$95.745^{+32.827}_{-25.304}$
13.001–17.421	4.420	15.211	1.864	1.000	10	$100.053^{+43.022}_{-31.017}$
17.421–23.344	5.923	20.382	1.864	1.000	8	$138.663^{+67.598}_{-48.532}$
23.344–31.281	7.937	27.312	1.864	1.000	8	$213.640^{+104.149}_{-74.774}$
31.281–41.916	10.635	36.598	1.864	1.000	4	$156.313^{+125.050}_{-74.249}$
41.916–56.168	14.251	49.042	1.864	1.000	4	$274.038^{+219.231}_{-130.168}$
56.168–75.264	19.097	65.716	1.864	1.000	2	$241.168^{+313.518}_{-156.759}$
75.264–100.854	25.590	88.059	–	–	–	–
100.854–135.145	34.290	118.000	–	–	–	–
135.145–181.094	45.949	158.119	–	–	–	–
181.094–242.666	61.572	211.880	1.864	1.000	1	$505.120^{+1161.775}_{-404.096}$
242.666–325.173	82.506	283.919	1.864	1.000	1	$685.387^{+1576.389}_{-548.309}$

Note. The listed counts were corrected for completeness and bias corrections (Resolution and Eddington Bias) (see the text for details).
(1) The flux density bins.
(2) The width of the flux density bins.
(3) The central flux density of the bin.
(4) The effective area corresponding to the bin centre.
(5) The Eddington bias correction factor.
(6) The number of sources in each flux density bin.
(7) The corrected normalized source counts.

Vaccari 2015) positions using a variable search radius equal to three times the combined astrometric error. Where a SERVS match was not found, we used the UKIRT Infrared Deep Sky Survey (UKIDSS) Deep Extragalactic Survey (DXS) DR10Plus data release (Lawrence et al. 2007). Both the SERVS and UKIDSS catalogues were astrometrically calibrated against 2MASS, which provide a dense and accurate astrometric reference frame. Radio positional errors for individual sources from PyBDSF source finder (Mohan & Rafferty 2015) are typically a few a tenths of an arcsecond. We computed the median astrometric offsets between the GMRT and SERVS catalogues to be $+0.539 \pm 0.420$ in RA and -0.327 ± 0.422 arcsec in RA and Dec., respectively, from an initial cross-matching. We applied these corrections to the radio positions before performing a second cross-matching. We measured a median astrometric offsets for the second cross-matching to be $+0.055 \pm 0.447$ in RA and -0.026 ± 0.435 in Dec. This correction was then applied to the radio positions for a final cross-matching. The radio positions within our final catalogue in Table 2 were corrected following this procedure are thus ultimately also registered against 2MASS.

Virtually all cases where a match was found resulted in a unique identification, given the sub-arcsecond accuracy of the positions. For all GMRT sources with a match in SERVS/UKIDSS we determined multi-wavelength properties using the SERVS Data Fusion workflow, i.e. matching all ancillary catalogues with a search radius of 1 arcsec against the SERVS/UKIDSS position.

Table 2. Sample of the source catalogue of GMRT 610 MHz sources. The columns are described in the text.

ID	RA (deg)	σ_{RA} (arcsec)	Dec. (deg)	$\sigma_{Dec.}$ (arcsec)	S_{int} (mJy)	$\sigma_{S_{int}}$ (mJy)	S_{peak} (mJy)	$\sigma_{S_{peak}}$ (mJy)	rms (mJy)	S_{code}	Type
(1)	(2)	(3)	(4)	(5)	(6)	(7)	(8)	(9)	(10)	(11)	(12)
1	243.801805	0.35	54.621228	0.36	0.2610	0.0555	0.2253	0.0290	0.0282	S	P
2	243.810522	0.04	54.993388	0.04	3.2388	0.0817	2.9474	0.0443	0.0435	S	E
3	243.797445	0.12	54.588408	0.10	0.7786	0.0478	0.6214	0.0237	0.0228	S	E
4	243.798035	0.40	54.594328	0.57	0.1594	0.0460	0.1432	0.0245	0.0242	S	P
5	243.802174	0.46	54.764238	0.74	0.2206	0.0654	0.1583	0.0298	0.0283	S	P
6	243.787447	0.18	54.310108	0.16	0.9742	0.0871	0.7077	0.0404	0.0383	S	E
7	243.801123	0.36	54.782338	0.30	0.1354	0.0379	0.1773	0.0260	0.0283	S	P
8	243.793715	0.34	54.539598	0.30	0.1761	0.0438	0.2095	0.0283	0.0297	S	P
9	243.808151	0.43	55.138628	0.64	0.7233	0.1393	0.3626	0.0488	0.0461	S	E
10	243.795284	0.46	54.718948	0.45	0.2611	0.0627	0.1945	0.0296	0.0280	S	P

Notes. The catalogue columns are as follows:
(1) GMRT 610 MHz Source ID.
(2) and (3) Flux-weighted right ascension (RA) and uncertainty.
(4) and (5) Flux-weighted declination (Dec.) and uncertainty.
(6–7) Integrated source flux density and uncertainty.
(8–9) Peak flux density and uncertainty.
(10) The average background rms value of the island.
(11) Code that defines the source structure. S – a single-Gaussian source that is the only source in the island. M – a multi-Gaussian source.
(12) Defines a source as extended (E) or point source (P).

Table 3. GMRT cross-matching statistics.

Category	Size	Fraction (per cent)
GMRT	4290	100
Matched	3689	92
SERVS	3689	86
UKIDSS	3542	83
SWIRE IRAC1234	1623	43
MIPS 24 μm	2714	63
X-ray	149	3
SPEC-Z[a]	834	19
PHOTZ-HSC[b]	2885	67
PHOTZ-SWIRE[c]	907	21
PHOTZ-HELP[d]	1834	43
REDSHIFT[e]	3105	72
CLASS[f]	3490	81
REDSHIFT & CLASS[g]	2304	54

Notes. [a]Spectroscopic redshifts.
[b]Hyper Suprime-Cam (HSC) Photometric Redshift Catalogue (Tanaka et al. 2018).
[c]SWIRE Revised Photometric Redshift Catalogue (Rowan-Robinson et al. 2008, 2013).
[d]HELP Photometric Redshift Catalogue (Duncan et al. 2018).
[e]The union of SPECZ, PHOTOZ-HSC, PHOTOZ-SWIRE, and PHOTOZ-HELP.
[f]All sources with at least one multiwavelength classification diagnostic.
[g]All sources with at least one multiwavelength classification diagnostic and redshift association.

This ancillary data include IRAC1234 and MIPS 24 μm photometry from SWIRE (Lonsdale et al. 2003), PACS, and SPIRE photometry from HerMES (Oliver et al. 2012) and redshift information. Table 2 shows a sample of 10 rows and a few selected columns from the curated catalogue with multiwavelength properties, which is available electronically in its entirety.

Table 3 summarizes the multiwavelength and redshift information available for the cross-matched GMRT sources, included in the SERVS Data Fusion catalogue. Accounting for multiple sources the final number of our GMRT 610 MHz sources is 4290. The redshift information is discussed in more detail in the following section. Table 4 provides the photometric redshift performance for GMRT radio sources as a function of i_{AB} optical magnitude.

Table 4. Photometric redshift performance for GMRT radio sources as a function of i_{AB} optical magnitude.

i_{AB}	σ_{NMAD}	O_f
[15.03, 19.62]	0.054	0.075
[19.62, 20.94]	0.047	0.017
[20.94, 22.21]	0.063	0.121
[22.21, 23.37]	0.044	0.035
[23.37, 24.47]	0.052	0.070
[24.47, 33.22]	0.035	0.098

4.2 Redshifts

We have combined the spectroscopic redshift compilations from the Spitzer Data Fusion[3] and HELP[4] projects to collect spectroscopic redshifts. The majority of the spectroscopic redshifts for our sample were obtained with the Baryon Oscillation Spectroscopic Survey (BOSS; Eisenstein et al. 2011). This is supplemented by a small number of redshifts available from the literature and from SWIRE/HerMES spectroscopic follow-up programme. For sources where a spectroscopic redshift was not available, we use photometric redshift estimates from the Hyper Suprime-Cam (HSC) project (Tanaka et al. 2018), the SWIRE project (Rowan-Robinson et al. 2008, 2013), and the HELP project (Duncan et al. 2018).

The redshift distribution is shown in Fig. 10 with the blue histogram representing spectroscopic redshifts and red histogram for photometric redshifts. We estimate the precision of the photometric redshifts using the normalized median absolute (i.e. deviation σ_{NMAD}; Hoaglin 2003), given by $1.48 \times \text{median}(|\Delta z|)/(1 + z_{spec})$. The second metric we estimate is the outlier fraction, O_f, defined as

[3]http://mattiavaccari.net/df/specz
[4]http://hedam.lam.fr/HELP/dataproducts/dmu23/

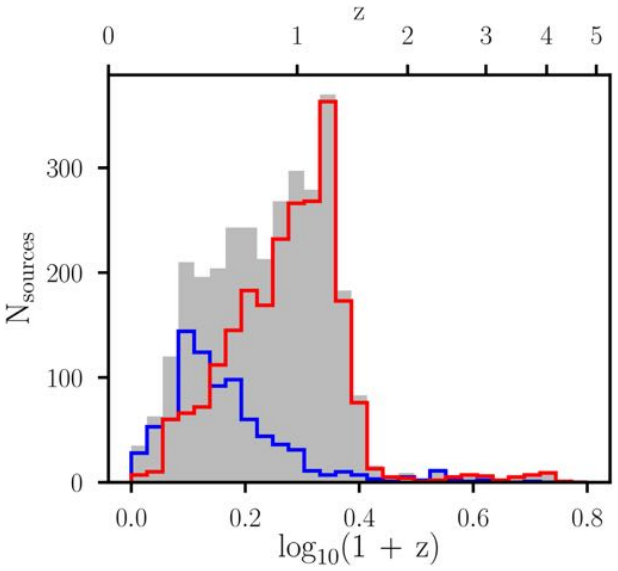

Figure 10. Redshift distribution for the GMRT 610 MHz sources. The grey histogram represents all the redshifts (i.e. both spectroscopic and photometric redshifts). The blue and red histograms represents spectroscopic and photometric redshifts, respectively.

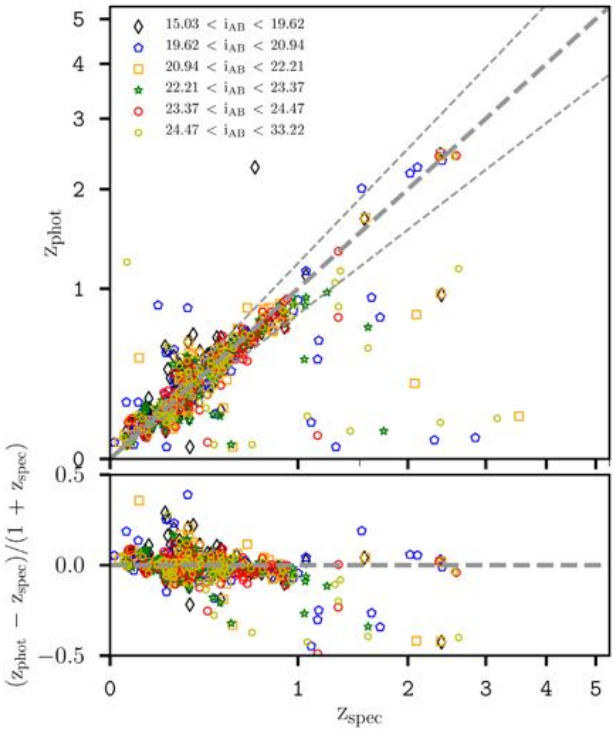

Figure 11. Comparison between photometric and spectroscopic redshifts as a function of i_{AB} magnitude in top panel. The dashed grey line corresponds to $z_{spec} = z_{phot}$. The double dashed lines show $z_{phot} = z_{spec} \pm 0.2(1 + z_{spec})$. The lower panel show $(z_{phot} - z_{spec})/(1 + z_{spec})$ versus z_{spec} as a function of i_{AB} magnitude.

$|\Delta z|/(1 + z_{spec}) > 0.2$ (see Brammer, van Dokkum & Coppi 2008; Dahlen et al. 2013; Laigle et al. 2016; Duncan et al. 2018). We use these metrics to explore the performance of the photometric redshift estimates relative to the measured spectroscopic redshift. Fig. 11 (upper panel) compares the photometric and spectroscopic redshift for different bins of i_{AB} magnitude for the GMRT sample. The bottom panel of Fig. 11 presents $(z_{phot} - z_{spec})/(1 + z_{spec})$ as a function of z_{spec}. The horizontal line in indicates where $(z_{phot} - z_{spec})/(1 + z_{spec}) = 0$. This plot clearly shows that the fraction of outliers increases significantly towards higher values of as a function of i_{AB} magnitude. The fraction of catastrophic failures varies from 3 to 9 per cent and the scatter, NMAD is nearly constant with an average value of NMAD = 0.049 for the entire spectroscopic sample. The scatter does increase above $z_{spec} > 1.5$, where $\sigma_{NMAD} = 0.075$. Systematic deviations from the $z_{phot} = z_{spec}$ line are very small at most redshifts, with the exception that z_{phot} underestimates z_{spec} at $z = 1.0-1.4$ by ~ 5 per cent.

4.3 AGN/SFG diagnostics overview

Following Ocran et al. (2017), we have carried out a multiwavelength study using optical, X-ray, infrared, and radio diagnostics to search for evidence of AGN-driven activity in our sample. The total number of sources with redshifts for which we can define at least one AGN indicator is 2305 (i.e. ~ 54 per cent of the whole sample and ~ 74 per cent of the subsample with redshifts). The AGN diagnostics we employed are described as follows:

(1) Radio power: We classify sources as RL AGNs based on a radio luminosity cut-off $L_{1.4\,GHz} \geq 10^{25}$ W Hz^{-1} (e.g. Sajina et al. 2007, 2008). We converted the 610 MHz radio flux densities to rest-frame 1.4-GHz effective luminosities, assuming a radio spectral index of $\alpha = -0.7$ (i.e. $S(\nu) \propto \nu^{\alpha}$; Ibar et al. 2010).[5]

(2) Mid-infrared to radio flux ratio: Following the Bonzini et al. (2013), we compute $q_{24\,\mu m}$ for the radio sources with MIPS 24μm detections and redshifts. This is then compared to the redshifted $q_{24\,\mu m}$ value for the M82 local standard starburst galaxy template. If $q_{24\,\mu m}$ is lower than the one expected for M82 (i.e. below -2σ, $\sigma = 0.35$ average spread for local sources by Sargent et al. 2010), the sources are considered as a RL AGN.

(3) X-ray luminosity: We classify a source as an AGN when $L_x > 10^{42}$ erg s^{-1} following e.g. Szokoly et al. (2004).[6]

(4) BOSS AGN spectroscopic classification: We use the BOSS CLASS and SUBCLASS parameters, as detailed by Bolton et al. (2012), to classify the GMRT sources with BOSS identifications. The breakdown of the BOSS CLASS and SUBCLASS parameters is outlined in Ocran et al. (2017).

(5) IRAC colours: We use the IRAC four-band colour–colour AGN diagnostic proposed by Donley et al. (2012):

$$x = \log_{10}\left(\frac{f_{5.8\,\mu m}}{f_{3.6\,\mu m}}\right), \quad y = \log_{10}\left(\frac{f_{8.0\,\mu m}}{f_{4.5\,\mu m}}\right), \tag{9}$$

$$\begin{aligned} &x \geq 0.08 \wedge y \geq 0.15, \\ &\wedge y \geq (1.21 \times x) - 0.27, \\ &\wedge y \leq (1.21 \times x) + 0.27, \\ &\wedge f_{4.5\,\mu m} > f_{3.6\,\mu m} > f_{4.5\,\mu m} \wedge f_{8.0\,\mu m} > f_{5.8\,\mu m}. \end{aligned} \tag{10}$$

Using these AGN/SFG indicators, we classify the 610 MHz sources as follows:

[5] $L_{1.4\,GHz} = 4\pi d_{lum}^2 \frac{S_{1.4\,GHz}}{(1+z)^{1+\alpha}}$, where $S_{1.4\,GHz} = \left(\frac{1.4}{0.61}\right)^{\alpha} S_{0.6\,GHz}$.

[6] $L_x = 4\pi S_x d_L^2 (1+z)^{2-\gamma}$, where we fixed the photon-index to the commonly observed value of $\gamma = 1.8$ (Dadina 2008; Vito et al. 2014).

Figure 12. Top: Nested donut chart with two groups illustrating the GMRT sample that is matched (92 per cent, green) and unmatched (8 per cent, violet) to SERVS/UKIDSS positions. The three subgroups represent the GMRT sample with redshift (72 per cent, dark grey), no redshift (20 per cent, light grey), and the unmatched (8 per cent, violet). Bottom: Nested donut chart with two groups illustrating the GMRT sample with redshift and at least one AGN indicator (54 per cent, green), redshift and no AGN indicator (46 per cent, violet). The four subgroups represents the fraction classified as SFG (36 per cent, dark grey), RL AGN (10 per cent, light grey), RQ AGN (8 per cent, violet), and redshift and no AGN indicator (46 per cent, violet).

(1) RL AGN: These are sources with redshift information and $L_{1.4\,\mathrm{GHz}} > 10^{25}$ W Hz^{-1} or $q_{24\mu\mathrm{m}}$ below the M82 locus.

(2) RQ AGN: Sources with redshifts and above the M82 locus threshold for selecting RL AGN. Furthermore, these sources are classified as AGN by at least one of the AGN diagnostics listed above.

(3) SFG: These are sources with redshifts that do not show evidence of AGN activity in any of the diagnostics.

(4) Unknown: These sources include those that are unmatched to SERVS IRAC12 positions, sources with no redshift, and sources with redshift but no information on the parameters needed for the AGN classification.

The top panel of Fig. 12 shows a nested donut chart with two groups illustrating the GMRT sources matched (92 per cent, lime) and unmatched (8 per cent, violet) to SERVS/UKIDSS positions. The three subgroups represents the GMRT sources with redshift (72 per cent, dark grey), no redshift (20 per cent, light grey), and unmatched (8 per cent, violet). The bottom panel represents a nested donut chart with two groups, illustrating the GMRT sources with redshift and AGN classification possible for at least one AGN diagnostics (54 per cent, green), redshift but no AGN classification possible (46 per cent, violet). The four subgroups represent the fraction classified as SFG (36 per cent, dark grey), RL AGN (10 per cent, light grey), RQ AGN (8 per cent, violet), and redshift and no AGN classification possible (46 per cent, violet).

The substantial number of objects in our sample allows us to study how the faint radio source population changes with flux density. The left-hand panel of Fig. 13 shows the fraction of objects in each class in our sample as a function of limiting flux density. For a given flux density, $S_{610\,\mathrm{MHz}}$, the plot shows the fraction of objects that are classified as SFG, RL AGN, and RQ AGN in the sample of objects above that flux density. The green curves show the fraction for the total AGN population. The curves highlight the dramatic change in population over this flux density range. The SFG fraction exhibits a monotonic increase with decreasing flux density from $\sim$ 10 to 72 per cent. RL AGNs decrease rapidly from being the dominant population above $\sim$ 1 mJy to the smallest fraction below $\sim$ 0.3 mJy. The fraction of RQ AGNs remains roughly constant with flux density just above $\sim$ 10 per cent. Above $\sim$ 0.7 mJy, the fraction of RQ AGNs is higher than that of SFGs. Padovani et al. (2015) identified 626 radio sources with redshifts and classified 55 per cent, 25 per cent, and 20 per cent as SFGs, RQ AGNs, and RL AGNs, respectively, from a deep 1.4-GHz sample, reaching a 32.5 μJy flux limit over 0.29 deg^2 of the ECDFS VLA image. They further confirmed the main results of Padovani et al. (2011) that AGNs dominate at large flux densities ($\gtrsim$1 mJy), but SFGs become the dominant population below $\approx$0.1 mJy. Bonzini et al. (2013) reported that SFGs represent 57 $\pm$ 3 per cent of the sub-millijansky sample are missing at high-flux densities but become the dominant population below $\approx$ 0.1 mJy, reaching 61 per cent at the survey limit. Radio-quiet AGNs represent 26 $\pm$ 6 per cent (or 60 per cent of all AGNs) of sub-millijansky sources, but their fraction appears to increase at lower flux densities, where they make up 73 per cent of all AGNs and $\approx$ 30 per cent of all sources at the survey limit, up from $\approx$ 6 per cent at $\approx$ 1 mJy. These results from previous observations are in good agreement with what we report. The fact that we find more SFGs at faint flux densities can be attributed to our survey going deeper than previous surveys. We compare our results to the relative fraction of AGN and SFG computed for T-RECS by Bonaldi et al. (2019; see dash–dotted green and black lines in both panels of Fig. 13) and find that the fraction of our classified sources do not agree with T-RECS. When we add the fraction of sources that have no classification to the SFGs fraction, we see that below $\sim$ 0.6 mJy our computed AGN and SFGs fraction agrees well with T-RECS (see the right-hand panel of Fig. 13). Table 5 presents the total number of AGNs (including RL and RQ AGNs) and SFGs with respect to sources with redshifts and AGN classification possible as well as the full GMRT sample.

5 MULTIFREQUENCY RADIO SPECTRAL INDICES

Radio spectral energy distributions (SEDs) provide useful information that can be used to differentiate between sources types according to their dominant emission mechanisms (Marsden et al. 2014). We computed the spectral index between 325 and 610 MHz; 610 and 1400 MHz; and 610 and 5000 MHz for our EN1 sample using the GMRT 325 MHz deep survey by Sirothia et al. (2009); the Faint Images of the Radio Sky at Twenty centimetres (FIRST) 1400 MHz survey by Becker et al. (1995); and the JVLA 5000 MHz Ultra Deep Survey by Taylor et al. (2014). Since the images mentioned above have different resolutions (see Table 6), special care must be taken when we analyse results based on different frequency-selected samples.

From the commonly used simple power-law model, a negative α is indicative of sources dominated by synchrotron emission, such as radio galaxies. An $\alpha \sim 0$ may indicate either a star-forming galaxy dominated by free–free emission optically thin or optically thick synchrotron emission in core-dominated AGNs. Inverted $\alpha > 0$ spectra in the GHz regime can be associated with very young compact sources (GPS) or to Advection-Dominated Accretion Flow (ADAF) sources (see e.g. Narayan & Yi 1994). Thus, radio spectra are useful in unveiling the physical processes in radio sources (Prandoni et al. 2010; Singh & Chand 2018).

5.1 Radio spectral index versus flux analysis

We investigate the spectral index properties of 610 MHz low-frequency-selected sources. We estimated the median and the error on the median using the median absolute deviation (MAD) estimator, as this is a more robust measure of the variability of a univariate sample of quantitative data than the standard deviation

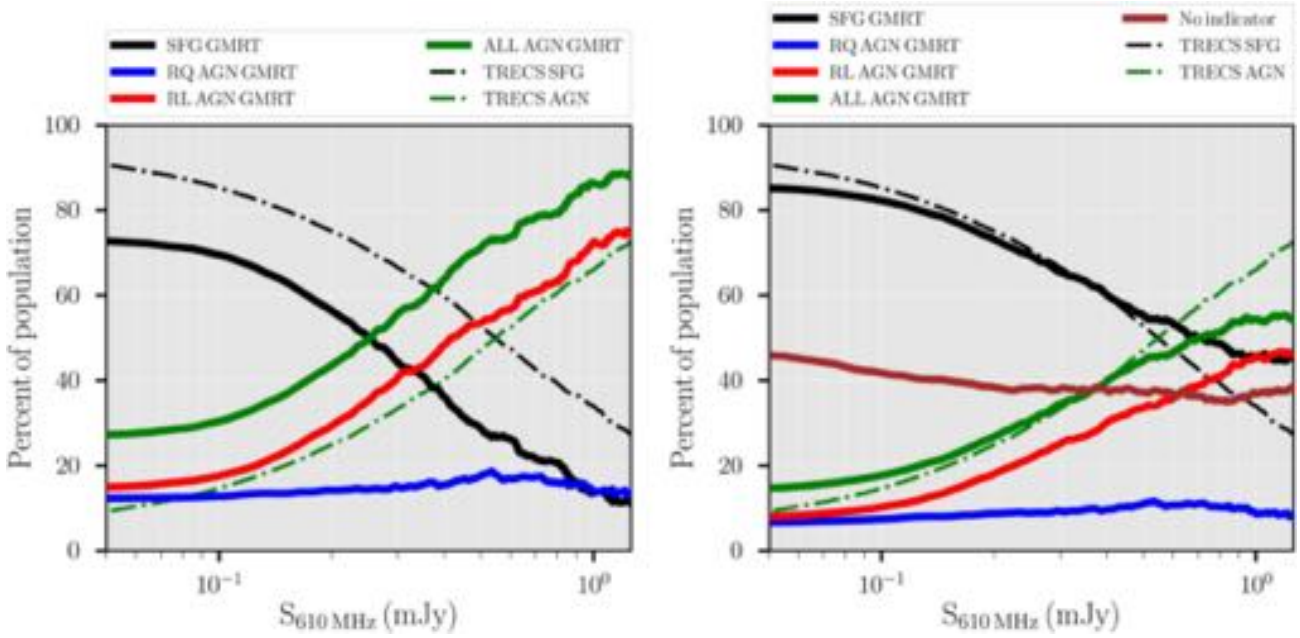

Figure 13. The relative fraction of AGNs and SFGs as a function of minimum flux density. The solid lines show the fraction of the sample with a flux density greater than $S_{610\,MHz}$ which is classified as RQ AGN (blue), RL AGN (red), all AGN (green), and SFG (black). The dashed dotted green and black lines in both panels represent the relative fraction of AGN and SFG predicted by T-RECS (Bonaldi et al. 2019).

Table 5. Total number of SFGs, RQ AGNs, and RL AGNs from the selection criteria.

Class	Number	Fraction (per cent) (sub-sample with redshift and class)	Fraction (per cent) (full sample)
SFG	1685	73	39
RQ AGN	281	12	7
RL AGN	338	15	8
No redshift or class	1986	–	46

Table 6. The radio surveys that were used to form the multifrequency samples through cross-matching with the 610 MHz catalogue.

Survey	Frequency (MHz)	Resolution (arcsec)	Area covered (deg^2)	rms (μJy)	Number of sources	Number of matches
EN1 GMRT Deep	325	10	1.5	70	901	479
VLA FIRST (All Sky)	1400	5	–	150	–	99
EN1 JVLA Deep	5000	2.5	0.12	1	387	204

(Rousseeuw & Croux 1993). Table 6 summarizes the number of matches between the 610 MHz catalogue and the samples at other frequency. Fig. 14 shows the 610–325, 610–1400, and 610–5000 MHz colour–flux diagrams. The distribution of the spectral index between each frequency pair is shown as blue histogram in each panel. For the top panel of Fig. 14, we note that only 479 of our GMRT 610 MHz sources have a counterpart at 325 MHz, therefore, α_{325}^{610} estimates are available only for 13 per cent of our radio-detected sources at 610 MHz. We find that α_{325}^{610} estimates range from −2.7 to 1.8 with a median value of -0.80 ± 0.29. Sirothia et al. (2009) reported a median spectral index between α_{325}^{610} 1.28 from 325 MHz studies of EN1 using the GMRT. They attributed their median value to an extra contribution of exceedingly steep diffuse emission being detected at the lower frequency. In the middle panel, only 99/4290 (∼ 2.3 per cent) of our 610 MHz detected sources have counterparts at 1.4 GHz. The α_{1400}^{610} estimates range from −2.5 to 1.1 with a median value of -0.83 ± 0.31. The bottom panel has the second highest number of sources, since the JVLA 5000 MHz Deep only covers an area of 0.12 deg^2 (see Table 6) and this is only a small region of the 610 MHz image. Only 204/4290 (∼4.8 per cent) of our 610 MHz sources have counterparts at 5 GHz with a median value of -1.12 ± 0.15.

At the lowest fluxes, we are only sensitive to increasingly steeper (top and middle panels) or flatter sources (bottom panel), hence the median values that we derive can be biased and unreliable. We therefore restrict our statistical analyses to a much brighter sub-sample and measure the median spectral index, where the red lines (see Fig. 14) are not biasing too much the median spectral indices. We find that the median spectral index for α_{325}^{610} for a flux range corresponding to $S_{610\,MHz} > 0.5$ mJy represented by the vertical black dash line in the top panel of Fig. 14 is -0.71 ± 0.27 (see the horizontal blue solid line). In the middle panel, we measure a median spectral index for α_{1400}^{610} over a flux range corresponding to $S_{610\,MHz} > 1.9$ mJy to be -0.89 ± 0.28 (see the horizontal blue solid

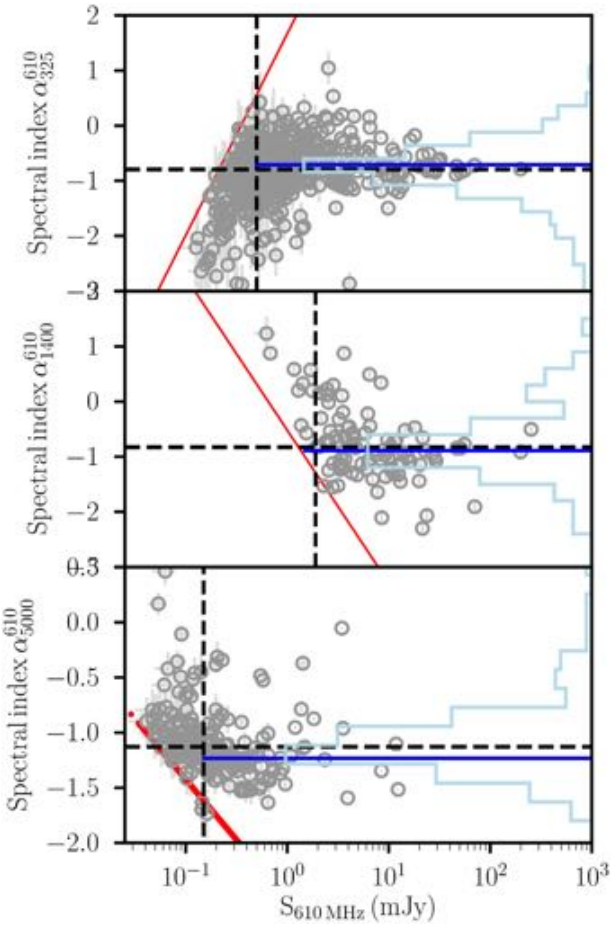

Figure 14. Colour–flux diagrams comparing the 325–610 MHz (top), 1400–610 MHz (middle), and 5000–610 MHz (bottom) spectral indices for EN1 GMRT Deep 610 MHz cross-identified sources. The solid red sloping line in each panel marks the flux density traced by the nominal detection limit of 325, 1400, and 5000 MHz, respectively (see Table 6). The distribution of the spectral index between each frequency is shown as blue histogram in each panel. The dashed vertical lines in each panel represent the flux limit we impose when restricting our statistical analyses to a much brighter sub-sample. The blue horizontal lines in each panel represent the median spectral indices we measure for sources above the imposed flux limits.

line). For the bottom panel, we measure a median spectral index for α_{5000}^{610} over a flux range corresponding to $S_{610\,\mathrm{MHz}} > 0.15$ mJy to be -1.23 ± 0.12 represented by the horizontal blue solid line.

The median spectral index α_{325}^{610} as a function of flux densities > 0.5 mJy is found to be approximately -0.71 from the original -0.80. This can be attributed to the fact that above the imposed flux density limit, most of the sources we select are AGNs and thus reduces the median spectral index we measure. The median spectral index α_{1400}^{610} is found to be approximately -0.83 to -0.89, based on an almost unbiased sources with flux densities > 1.9 mJy. Statistical analyses of Ibar et al. (2009) showed no clear evolution for the median spectral index, α_{1400}^{610}, as a function of flux density and that α_{1400}^{610} was found to be approximately -0.6 to -0.7 based on an almost unbiased 10σ criterion, down to a flux level of $S_{1.4\,\mathrm{GHz}} \gtrsim 100\,\mu$Jy. Katgert & Spinrad (1974) found from a small sample of sources with $S_{610\,\mathrm{MHz}} \gtrsim 10$ mJy a spectral index distribution of $\alpha_{1400}^{610} = -0.52 \pm 0.39$ using the Westerbork Synthesis Radio Telescope (WSRT). With respect to higher frequency surveys with a broad distribution, this was an unusual result. However, Katgert (1979) using a much larger sample presented similar result of $\alpha_{1400}^{610} = -0.68 \pm 0.31$. A detailed spectral index analysis using the other available radio data and adding the upper/lower limits for each source to get reliable estimates of median spectral indices through survival analysis is deferred to later works.

For the remaining 419/901 (∼47 per cent, for 325 MHz), 688/818 (∼84 per cent, for 1400 MHz), 170/330 (∼ 52 per cent, for 5000 MHz) detected with no counterparts in the GMRT 610 MHz, we derive the nominal detection limit in 325, 1400, and 5000 MHz (see Table 6), respectively, represented by the solid red line in each panel.

5.2 Radio colour–colour plot

Fig. 15 shows radio colour–colour plots for the EN1 GMRT 610 MHz Deep sample. The spectral indices of the sample between 325 and 610 MHz against the spectral indices between 1400 and 610 MHz (i.e. using the spectral indices measure in the middle panel of Fig. 14) is shown in the left-hand panel. The right-hand panel shows the spectral indices of the sample between 325 and 610 MHz against the spectral indices between 5000 and 610 MHz. We divide the radio colour–colour plot into four quadrants:

(1) Steep and flat spectrum sources: where ($\alpha_{1400}^{610} \mid \alpha_{5000}^{610} \leq 0$ and $\alpha_{325}^{610} \leq 0$)
(2) Peaked spectrum sources: where ($\alpha_{1400}^{610} \mid \alpha_{5000}^{610} \leq 0$ and $\alpha_{325}^{610} > 0$)
(3) Inverted spectrum sources: where ($\alpha_{1400}^{610} \mid \alpha_{5000}^{610} > 0$ and $\alpha_{325}^{610} > 0$)
(4) Upturn spectrum sources: where ($\alpha_{1400}^{610} \mid \alpha_{5000}^{610} > 0$ and $\alpha_{325}^{610} \leq 0$)

It is evident that the majority of our GMRT 610 MHz sources lie in the steep and flat-spectrum quadrant in both panels. Moreover, the scatter around the diagonal line is asymmetric for the first panel (i.e. α_{1400}^{610} versus α_{325}^{610}) of Fig. 15 with relatively more number of sources lying below the lower left side of the diagonal line (i.e. at $\alpha_{1400}^{610} < \alpha_{325}^{610}$), indicating a steepening of the spectrum at higher frequencies (despite the fact the α_{1400}^{610} MHz sample is biased towards flat spectrum sources. This is consistent with the RL AGN classification of most such sources).

The right-hand panels show a slight scatter around the diagonal. It is interesting to note that sources lying below the diagonal line (i.e. $\alpha_{325}^{610} < \alpha_{5000}^{610}$) are mostly SFGs or RQ AGNs. This sample has more SFGs as it is created from the deep, narrow 5000 MHz survey (see Table 6). In the first case, the flattening of the spectrum going at higher frequency may be due to an increase of the free–free emission contribution at high frequency; in the case of RQ AGN, the flattening may be due to the emergence of core-dominated emission.

5.3 SFG and AGN spectral indices

The distribution of the spectral index between α_{325}^{610} and α_{1400}^{610} for SFG and AGN is shown as black and green histograms in Fig. 16. The distribution for α_{325}^{610} is computed over a flux range corresponding to $S_{610\,\mathrm{MHz}} > 0.5$ mJy and that of α_{1400}^{610} is computed over a flux range corresponding to $S_{610\,\mathrm{MHz}} > 1.5$ mJy, respectively. From Fig. 16, the median and MAD computed over $S_{610\,\mathrm{MHz}} > 0.5$ mJy is $\langle\alpha_{325}^{610}\rangle = -0.81 \pm 0.23$ for SFGs and $\langle\alpha_{325}^{610}\rangle = -0.69 \pm 0.22$ for AGNs. RL and RQ AGNs have a median and MAD of $\langle\alpha_{325}^{610}\rangle = -0.67 \pm 0.27$ and $\langle\alpha_{325}^{610}\rangle = -0.71 \pm 0.22$, respectively.

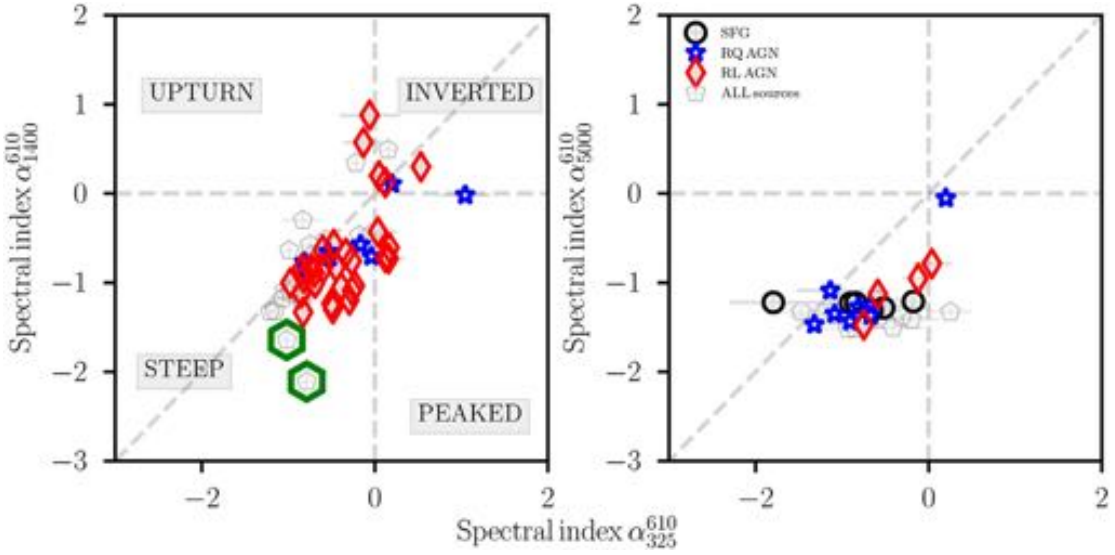

Figure 15. Radio colour–colour plots for sources the EN1 GMRT 610MHz Deep sample. Left: The spectral indices of the sample between 325 and 610 MHz against the spectral indices between 1400 and 610 MHz. Right: The spectral indices of the sample between 325 and 610 MHz against the spectral indices between 5000 and 610 MHz. SFG, RQ AGN, RL AGN, and all sources indicator are represented with black, red, blue, and dimgrey colours, respectively. The green hexagon in the left-hand panel shows ultra very steep sources (i.e. $\alpha^{610}_{1400} < -1.5$).

We computed $\langle\alpha^{610}_{1400}\rangle = -0.81 \pm 0.26$ over $S_{610\,\mathrm{MHz}} > 1.9$ mJy for AGNs (see the bottom panel of Fig. 16). In addition, RL and RQ AGNs have a median and MAD of $\langle\alpha^{610}_{1400}\rangle = -0.89 \pm 0.28$ and $\langle\alpha^{610}_{1400}\rangle = -0.68 \pm 0.10$, respectively. The number of SFGs having α^{610}_{1400} associations is only one and not included in this analysis. Table 7 shows the breakdown of the number of SFGs, RL AGN, RQ AGN, and sources with no classification that have a spectral index.

5.4 Ultra-steep spectrum sources

Ultra-steep spectrum sources (USS) radio sources are often associated with radio galaxies at high redshift (HzRGs z > 2) (e.g. see Blumenthal & Miley 1979; Miley & De Breuck 2008). HzRGs are located in overdense regions in the early Universe and are frequently surrounded by protoclusters (Roettgering et al. 1996; Pascarelle et al. 1996; Knopp & Chambers 1997). Studies have shown USS are good candidates for high-redshift radio galaxies (Riseley et al. 2016) that are among the most luminous and massive galaxies (e.g. De Breuck & Reuland 2005; Bornancini et al. 2007; Singh et al. 2014) and are believed to be progenitors of the massive elliptical galaxies in the local universe. Their extremely steep spectrum is generally attributed to radiation losses of relativistic electrons in the radio lobes, meaning they are most luminous at lower radio frequencies (Mahony et al. 2016).

In the literature, USS radio sources are commonly defined as those with spectral index values $\alpha < -1.3$ (Argo et al. 2013; Herzog et al. 2016). We selected sources that had spectral indices between 610 MHz and 1.4 GHz steeper than $\alpha^{610}_{1400} = -1.2$. Using this criterion, we find two sources with ultra-steep spectra in the GMRT 610 MHz sample. The 610–325 MHz spectral index for the first USS candidate (i.e source with GMRT ID 713) is $\alpha^{610}_{325} = -1.01$, whereas the 610–1400 MHz spectral index is $\alpha^{610}_{1400} = -1.65$. The second USS candidate (i.e source with GMRT ID 2388) has a 610–325 MHz spectral index of $\alpha^{610}_{325} = -0.79$ and a 610- to 1400 MHz spectral index of $\alpha^{610}_{1400} = -2.10$. This source is at the detection of threshold of the NRAO VLA Sky Survey (NVSS) (Condon et al. 1998) and has flux density of 2.1 ± 0.4 mJy at 1.4 GHz. If we use this flux, then 610–1400 MHz spectral index is $\alpha^{610}_{1400} = -1.6$. Both candidate USS sources do not have redshift associations in our catalogue, hence these sources are more likely to be HzRGs.

Fig. 17 shows the flux density as a function of frequency for the two very steep spectrum sources identified in Fig. 15, the two-point spectral index values are also printed on the figure. Postage stamp images of these sources are presented in Fig. 18.

6 SUMMARY AND CONCLUSIONS

We report deep 610 MHz GMRT observations of the EN1 field, a region of 1.864 deg^2. We achieve a nominal sensitivity of 7.1 μJy beam^{-1}. From our 610 MHz mosaic image, we recover 4290 sources after accounting for multiple component sources down to a 5σ flux density limit of 35.5 μJy.

From this data, we derive the 610 MHz source counts applying corrections for completeness, resolution bias, and Eddington bias. The counts are within the scatter of most previous source counts from other surveys at 610 MHz and with extrapolated models of the low-frequency source population; the most obvious exception is the Wilman et al. (2008) source counts. The counts show a flattening below ∼ 1 mJy as a result of the increasing contribution of SFGs (Rawlings & Jarvis 2004; Padovani et al. 2015; Padovani 2016b).

Our radio catalogue was cross-matched against SERVS, UKIDSS, and other multiwavelength data sets. Using the different radio, mid-infrared, optical, and X-ray AGN indicators explored in Ocran et al. (2017), we have efficiently separated the radio source population with redshift into three classes: SFGs, RQ AGNs, and RL AGNs. The relative contribution of the three classes of sources to the sub-sample of radio sources with redshifts and at least one multiwavelength diagnostic is as follows: ∼73 per cent SFGs, ∼12 per cent RQ AGNs, and ∼15 per cent RL AGNs. Compared to our previous analysis over a smaller area at 610 MHz in the same field, our results indicate a continued increase in the relative fraction of SFGs with decreasing flux density. Ocran et al. (2017)

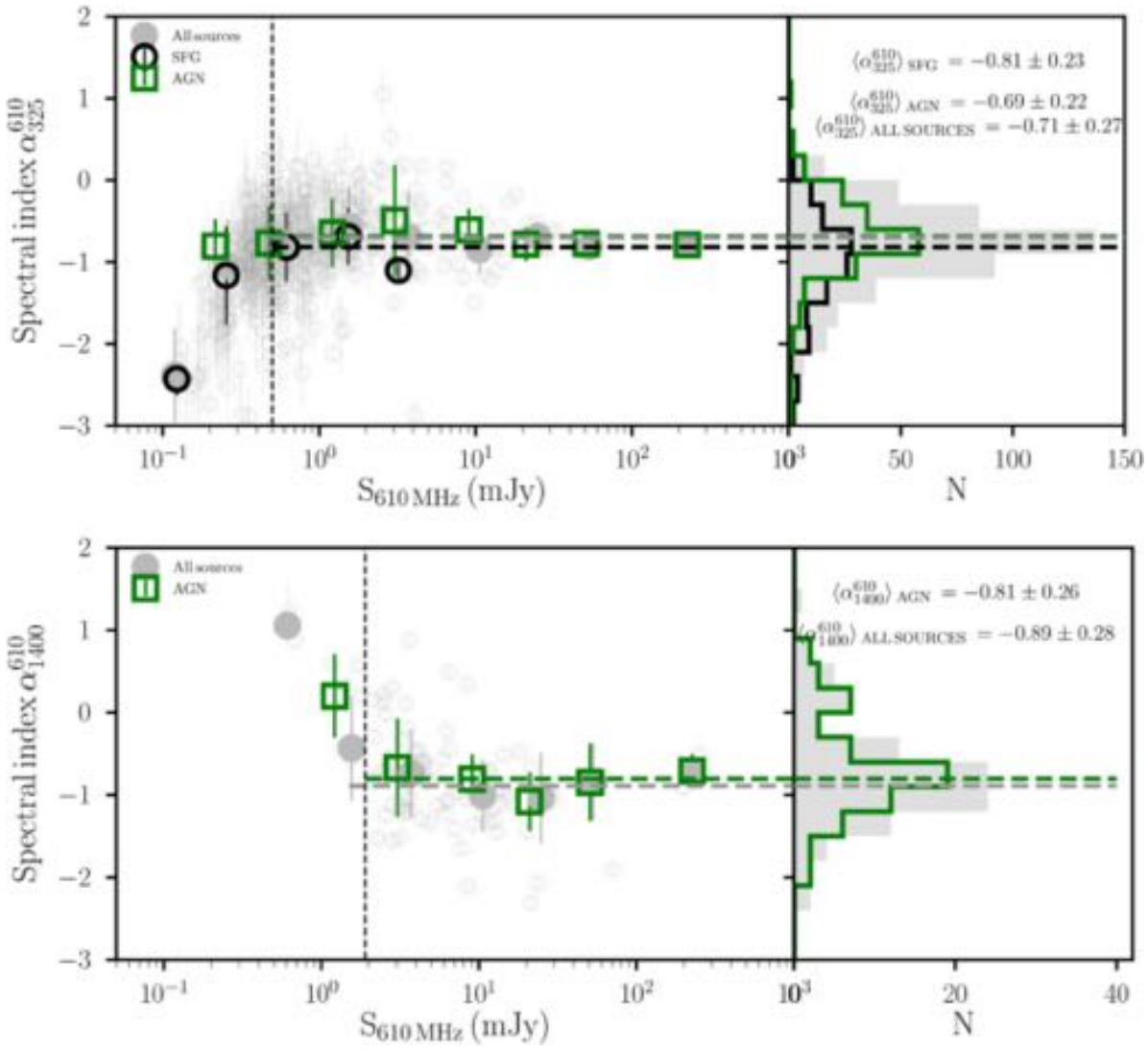

Figure 16. Top panel: The distribution for α^{610}_{325} is computed over a flux range corresponding to $S_{610\,\rm MHz} > 0.5$ mJy. The filled grey circles, open black circles, and open green squares represent all sources, SFGs, and AGNs, respectively, in logarithmic bins of 0.4. Bottom panel: The distribution for α^{610}_{1400} is computed over a flux range corresponding to $S_{610\,\rm MHz} > 1.9$ mJy. The filled grey circles and open green squares represent all sources and AGNs, respectively, in logarithmic bins of 0.4. The number of SFGs having α^{610}_{1400} associations is only one and not included in the plot.

Table 7. Number of SFGs, RL AGN, RQ AGN, and sources with no classification that have a spectral index.

α	SFG	RL AGN	RQ AGN	No classification
α^{610}_{325}	122	125	48	184
α^{610}_{1400}	1	53	10	35
α^{610}_{5000}	73	12	23	96

reported that RQ AGNs dominate the AGN population but in this work spanning a larger area of the same field we conclude that RL AGNs actually dominate. The significantly higher fraction of SFGs in our sample may also partially arise from the selection at lower frequency, where at a given flux density threshold flat-spectrum AGN cores are preferentially detected at 1.4 GHz.

We matched our 610 MHz catalogue and compared with catalogues from other surveys at different frequencies. In this regard, we form a sample with which to study the spectral index properties of low-frequency radio sources. We measure the median spectral index between 610 and 325 MHz; 610 and 1400 MHz; and 610 and 5000 MHz. Our sample is dominated by steep-spectrum sources as expected for low-frequency-selected sources. We measure a median spectral index of $\alpha^{610}_{325} = -0.80 \pm 0.29$, $\alpha^{610}_{1400} = -0.83 \pm 0.31$, and $\alpha^{610}_{5000} = -1.12 \pm 0.15$. We note that the median spectral index we measure at other frequencies for our sample is currently severely limited by the sensitivity of the high-frequency reference. The radio colour–colour plot (i.e. α^{610}_{1400} versus α^{610}_{325}) reveals a steepening which is consistent with our RL AGN classification. Massardi et al. (2011) showed that a spectral index of $\alpha = 0.5$ provides a clean way of distinguishing flat-spectrum/compact sources from steep-spectrum/extended sources. These extended sources emit synchrotron radiation at relatively high frequencies, where they are optically thin, implying the existence of fast electrons moving in a magnetic field which is a signature of RL AGN (see Padovani 2016b). Thus, the steepening of our RL AGN sources can be attributed to the systematic increase in the synchrotron age of

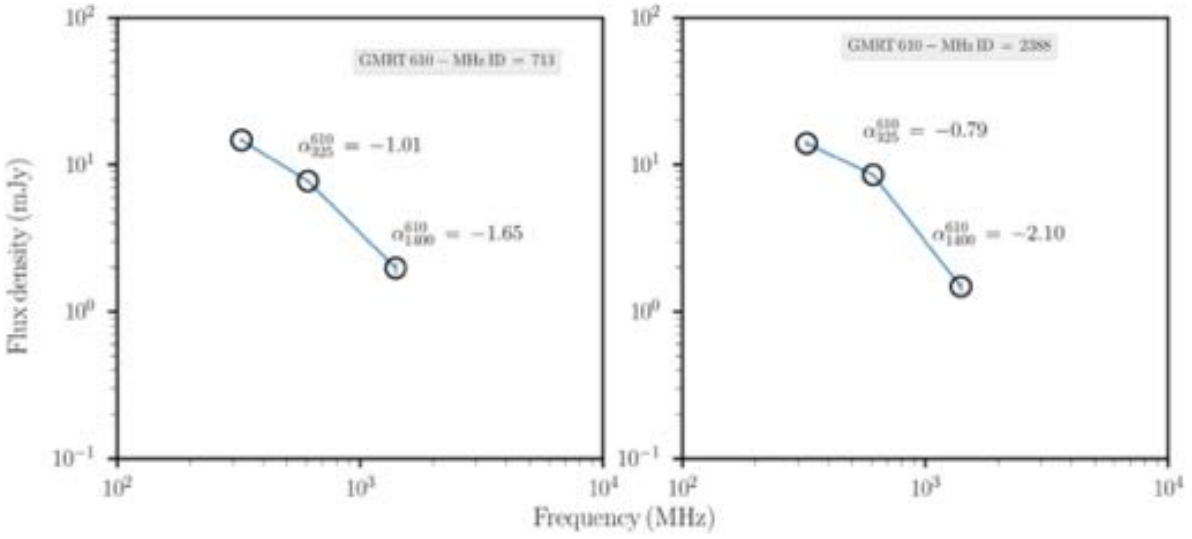

Figure 17. Flux density as a function of frequency for the two ultra-steep spectrum sources identified in Fig. 15. The radio SED for the two USS is from 325 to 1400 MHz. Also shown are the spectral indices measured between data available for this source at various radio frequencies.

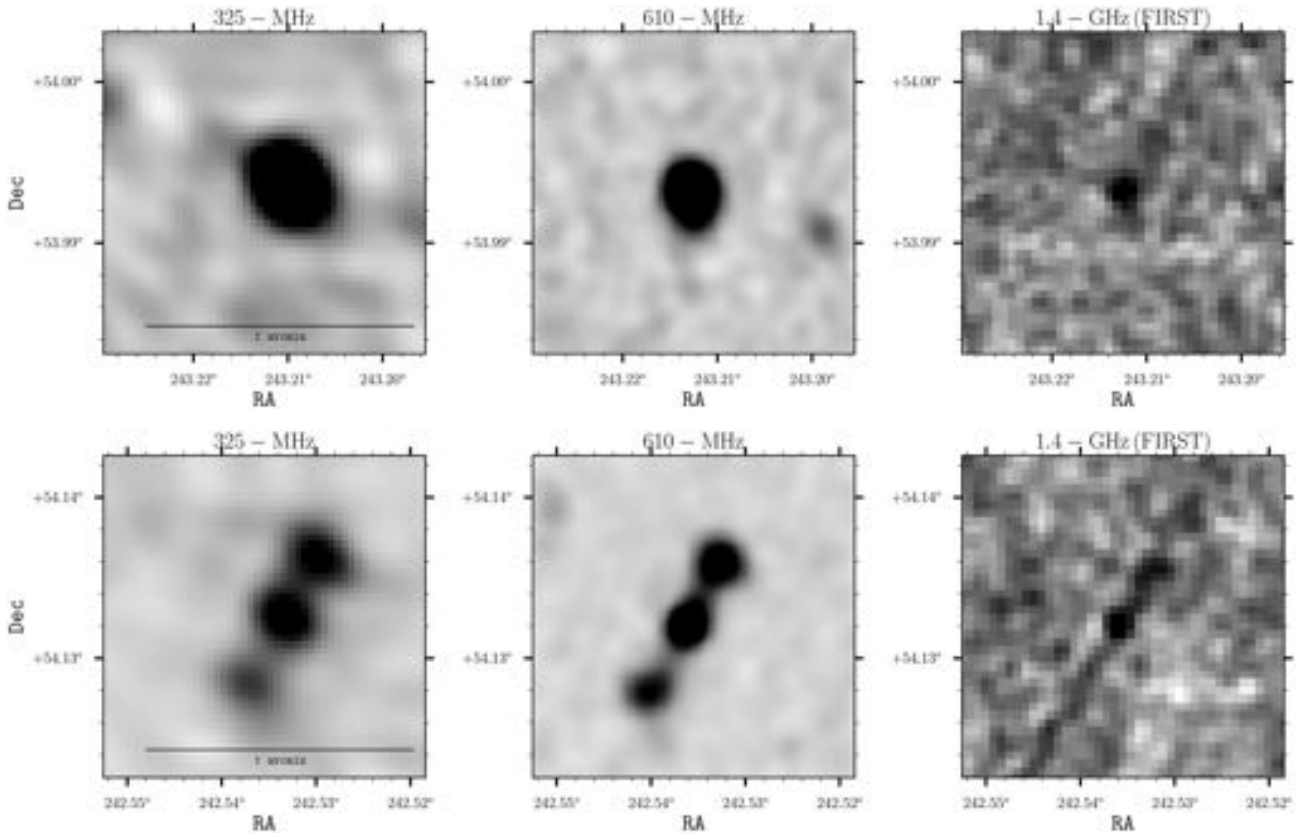

Figure 18. Candidate USS radio sources at three different frequencies from 325 , 610, and 1.4 GHz (FIRST), respectively, for the two sources.

the relativistic jets extending well beyond the host galaxy, i.e. an increase from the lobes' head towards their flaring ends (see Sadler, Jenkins & Kotanyi 1989; Machalski, Jamrozy & Konar 2010).

Restricting our statistical analyses to a much brighter sub-sample, $S_{610\,MHz} > 0.5$ mJy for α_{325}^{610} and $S_{610\,MHz} > 1.9$ mJy for α_{1400}^{610}, we measure a -0.71 and -0.89, respectively. The median spectral indices between 610 and 325 MHz of the bright sample for SFGs and AGNs is -0.81 ± 0.23 and -0.69 ± 0.22, respectively. We also measure a median spectral index between 610 and 1400 MHz of -0.81 ± 0.26 for AGNs over $S_{610\,MHz} > 1.9$ mJy.

By adopting the definition of a USS object as a radio source with $\alpha < -1.3$, we find a total of two USS radio sources. The two candidate USS sources have no corresponding redshift association (both spectroscopic and photometric) from the multiwavelength catalogue (see Sections 4 and 4.2) and therefore remain unclassified.

Saxena et al. (2018a) defined a sample of USS radio sources from the TGSS ADR1 at 150 MHz to search HzRGs. They used the TGSS along with FIRST and NVSS at 1.4 GHz to select sources with spectral indices steeper than −1.3 resulting in a final sample consisting of 32 sources. Currently, most powerful distant radio galaxy is at $z = 5.7$ (Saxena et al. 2018b) with an ultra-steep spectral index, $\alpha_{1.4\,\mathrm{GHz}}^{150\,\mathrm{MHz}} = -1.4$ (see Saxena et al. 2018a). Although we have no redshift estimates for our two candidate USS sources, chances of them being HzRGs is very high. However, there is also the possibility of their being dust obscured radio AGNs at lower redshifts, low luminosity RQ AGNs that are pretty much indistinguishable from SFGs in terms of the radio emission at lower redshifts present in our sample. Follow-up observations are essential to confirm that the two USS sources are HzRGs.

A detailed and more complete analysis of the evolutionary properties of the different classes of sources in our GMRT sample, in comparison with other observational and modelling work will be the subject of forthcoming papers. Upcoming large radio continuum surveys with the SKA pathfinders and precursors (Norris et al. 2013), such as the MeerKAT International GHz Tiered Extragalactic Exploration (MIGHTEE) Survey (Jarvis et al. 2016) with MeerKAT (Jonas & MeerKAT Team 2016), will detect millions of radio sources down to fainter flux limits than we explored in this paper. It is therefore extremely important to be able to predict which kind of sources these facilities will observe and what are the key data in other spectral windows necessary to complement the radio information to maximize the scientific outputs of these projects. This work is particularly useful for paving the way to upcoming radio surveys that these new radio facilities will provide.

ACKNOWLEDGEMENTS

We thank the staff of the GMRT that made these observations possible. GMRT is run by the National Centre for Radio Astrophysics of the Tata Institute of Fundamental Research. We also thank Claudia Mancuso and Anna Bonaldi for providing us their model predictions. EFO thanks the anonymous referee for their comments on the manuscript. This work is based in part on observations made with the *Spitzer Space Telescope*, which is operated by the Jet Propulsion Laboratory, California Institute of Technology under a contract with NASA. We acknowledge support from the Italian Ministry of Foreign Affairs and International Cooperation (MAECI grant no. ZA18GR02) and the South African Department of Science and Technology's National Research Foundation (DST-NRF grant no. 113121) as part of the ISARP RADIOSKY2020 Joint Research Scheme.

REFERENCES

Argo M. K., Paragi Z., R'ottgering H.-R., Kl'ockner H.-R., Miley G., Mahmud M., 2013, MNRAS, 431, L58
Athreya R. M., Kapahi V. K., 1998, JA&A, 19, 63
Banfield J. K., George S. J., Taylor A. R., Stil J. M., Kothes R., Scott D., 2011, ApJ, 733, 69
Becker R. H., White R. L., Helfand D. J., 1995, ApJ, 450, 559
Best P. N. et al., 1998, MNRAS, 301, L15
Best P. N., Arts J. N., Röttgering H. J. A., Rengelink R., Brookes M. H., Wall J., 2003, MNRAS, 346, 627
Blumenthal G., Miley G., 1979, A&A, 80, 13
Blundell K. M., Kuncic Z., 2007, ApJ, 668, L103
Bolton A. S. et al., 2012, AJ, 144, 144
Bonaldi A., Bonato M., Galluzzi V., Harrison I., Massardi M., Kay S., De Zotti G., Brown M. L., 2019, MNRAS, 482, 2
Bondi M. et al., 2007, A&A, 463, 519
Bonzini M., Padovani P., Mainieri V., Kellermann K. I., Miller N., Rosati P., Tozzi P., Vattakunnel S., 2013, MNRAS, 436, 3759
Bornancini C. G., De Breuck C., de Vries W., Croft S., van Breugel W., Röttgering H., Minniti D., 2007, MNRAS, 378, 551
Brammer G. B., van Dokkum P. G., Coppi P., 2008, ApJ, 686, 1503
Braun R., Bourke T., Green J. A., Keane E., Wagg J., 2015, Proc. Sci., Advancing Astrophysics with the Square Kilometre Array. SISSA, Trieste, PoS(AASKA14)174
Condon J. J., 1984, ApJ, 287, 461
Condon J. J., 1992, ARA&A, 30, 575
Condon J. J., Cotton W. D., Greisen E. W., Yin Q. F., Perley R. A., Taylor G. B., Broderick J. J., 1998, AJ, 115, 1693
Dadina M., 2008, A&A, 485, 417
Dahlen T. et al., 2013, ApJ, 775, 93
De Breuck C., Reuland M., 2005, in Renzini A., Bender R., eds, Multiwavelength Mapping of Galaxy Formation and Evolution, ESO Astrophysics Symposia. Springer, Berlin, Heidelberg, p. 374
de Zotti G., Massardi M., Negrello M., Wall J., 2010, A&A Rev., 18, 1
Donley J. L. et al., 2012, ApJ, 748, 142
Duncan K. J., Jarvis M. J., Brown M. J. I., Röttgering H. J. A., 2018, MNRAS, 477, 5177
Eddington A. S., 1913, MNRAS, 73, 359
Eisenstein D. J. et al., 2011, AJ, 142, 72
Fomalont E. B., Kellermann K. I., Wall J. V., Weistrop D., 1984, Science, 225, 23
Garn T., Green D. A., Riley J. M., Alexander P., 2008, MNRAS, 383, 75
Gehrels N., 1986, ApJ, 303, 336
Grant J. K., Taylor A. R., Stil J. M., Land ecker T. L., Kothes R., Ransom R. R., Scott D., 2010, ApJ, 714, 1689
Gruppioni C. et al., 1999, MNRAS, 305, 297
Herzog A. et al., 2016, A&A, 593, A130
Heywood I. et al., 2016, MNRAS, 460, 4433
Hoaglin D. C., 2003, Stat. Sci., 18, 311
Ibar E., Ivison R. J., Biggs A. D., Lal D. V., Best P. N., Green D. A., 2009, MNRAS, 397, 281
Ibar E., Ivison R. J., Best P. N., Coppin K., Pope A., Smail I., Dunlop J. S., 2010, MNRAS, 401, L53
Intema H. T., van Weeren R. J., Röttgering H. J. A., Lal D. V., 2011, A&A, 535, A38
Intema H. T., Jagannathan P., Mooley K. P., Frail D. A., 2017, A&A, 598, A78
Jarvis M. et al., 2016, Proc. Sci., The MeerKAT International GHz Tiered Extragalactic Exploration (MIGHTEE) Survey. SISSA, Trieste, PoS(MeerKAT2016)006
Jarvis M. J., Rawlings S., Willott C. J., Blundell K. M., Eales S., Lacy M., 2001, MNRAS, 327, 907
Jonas J., MeerKAT Team, 2016, Proc. Sci., The MeerKAT Radio Telescope. SISSA, Trieste, PoS(MeerKAT2016)001
Katgert J. K., 1979, A&A, 73, 107
Katgert J. K., Spinrad H., 1974, A&A, 35, 393
Kellermann K. I., Wall J. V., 1987, in Hewitt A., Burbidge G., Fang L. Z., eds, Proc. IAU Symp. 124, Observational Cosmology. p. 545
Knopp G. P., Chambers K. C., 1997, ApJ, 487, 644
Laigle C. et al., 2016, ApJS, 224, 24
Lawrence A. et al., 2007, MNRAS, 379, 1599
Lonsdale C. J. et al., 2003, PASP, 115, 897
Machalski J., Jamrozy M., Konar C., 2010, A&A, 510, A84
Magliocchetti M., Andreani P., Zwaan M. A., 2008, MNRAS, 383, 479
Mahony E. K. et al., 2016, MNRAS, 463, 2997
Mancuso C. et al., 2017, ApJ, 842, 95
Marsden D. et al., 2014, MNRAS, 439, 1556
Massardi M., Bonaldi A., Negrello M., Ricciardi S., Raccanelli A., de Zotti G., 2010, MNRAS, 404, 532
Massardi M. et al., 2011, MNRAS, 412, 318
Mauduit J.-C. et al., 2012, PASP, 124, 714

Miley G., De Breuck C., 2008, A&AR, 15, 67
Mohan N., Rafferty D., 2015, Astrophysics Source Code Library, record ascl:1502.007
Moss D., Seymour N., McHardy I. M., Dwelly T., Page M. J., Loaring N. S., 2007, MNRAS, 378, 995
Narayan R., Yi I., 1994, ApJ, 428, L13
Norris R. P. et al., 2013, PASA, 30, e020
O'Dea C. P., 1998, PASP, 110, 493
Ocran E. F., Taylor A. R., Vaccari M., Green D. A., 2017, MNRAS, 468, 1156
Oliver S. J. et al., 2012, MNRAS, 424, 1614
Padovani P., 2016a, A&AR, 24, 13
Padovani P., 2016b, A&AR, 24, 13
Padovani P., Mainieri V., Tozzi P., Kellermann K. I., Fomalont E. B., Miller N., Rosati P., Shaver P., 2009, ApJ, 694, 235
Padovani P., Miller N., Kellermann K. I., Mainieri V., Rosati P., Tozzi P., 2011, ApJ, 740, 20
Padovani P., Bonzini M., Kellermann K. I., Miller N., Mainieri V., Tozzi P., 2015, MNRAS, 452, 1263
Pascarelle S. M., Windhorst R. A., Keel W. C., Scoville N., Armus L., 1996, American Astronomical Society Meeting Abstracts, p. 1386
Prandoni I., Gregorini L., Parma P., de Ruiter H. R., Vettolani G., Wieringa M. H., Ekers R. D., 2001, A&A, 365, 392
Prandoni I., Parma P., Wieringa M. H., de Ruiter H. R., Gregorini L., Mignano A., Vettolani G., Ekers R. D., 2006, A&A, 457, 517
Prandoni I., de Ruiter H. R., Ricci R., Parma P., Gregorini L., Ekers R. D., 2010, A&A, 510, A42
Rawlings S., Jarvis M. J., 2004, MNRAS, 355, L9
Riseley C. J. et al., 2016, MNRAS, 462, 917
Roettgering H. J. A., Lacy M., Miley G. K., Chambers K. C., Saunders R., 1994, A&AS, 108, 79
Roettgering H. J. A., Lacy M., Miley G. K., Chambers K. C., Saunders R., 1996, VizieR Online Data Catalog, 410
Rousseeuw P. J., Croux C., 1993, J. Am. Stat. Assoc., 88, 1273
Rowan-Robinson M. et al., 2004, MNRAS, 351, 1290
Rowan-Robinson M. et al., 2008, MNRAS, 386, 697
Rowan-Robinson M., Gonzalez-Solares E., Vaccari M., Marchetti L., 2013, MNRAS, 428, 1958
Sadler E. M., Jenkins C. R., Kotanyi C. G., 1989, MNRAS, 240, 591
Sajina A., Yan L., Lacy M., Huynh M., 2007, ApJ, 667, L17
Sajina A. et al., 2008, ApJ, 683, 659
Sargent M. T. et al., 2010, ApJ, 714, L190
Saxena A. et al., 2018a, MNRAS, 475, 5041
Saxena A. et al., 2018b, MNRAS, 480, 2733
Seymour N. et al., 2008, MNRAS, 386, 1695
Singh V., Chand H., 2018, MNRAS, 480, 1796
Singh V. et al., 2014, A&A, 569, A52
Sirothia S. K., Dennefeld M., Saikia D. J., Dole H., Ricquebourg F., Roland J., 2009, MNRAS, 395, 269
Smolčić V. et al., 2017, A&A, 602, A1
Snellen I. A. G., Schilizzi R. T., van Langevelde H. J., 2000, MNRAS, 319, 429
Szokoly G. P. et al., 2004, ApJS, 155, 271
Tanaka M. et al., 2018, PASJ, 70, S9
Taylor A. R. et al., 2014, in Chengalur J. N., Gupta Y., eds, ASI Conf. Ser. Vol. 13, The Metrewavelength Sky. Bulletin of the Astronomical Society of India (BASI), Pune, India, p. 99
Vaccari M., 2015, Proc. Sci., The Spitzer Data Fusion: Contents, Construction and Applications to Galaxy Evolution Studies. SISSA, Trieste, PoS(EXTRA–RADSUR2015)027
Vaccari M. et al., 2005, MNRAS, 358, 397
Vaccari M. et al., 2010, A&A, 518, L20
Vito F., Gilli R., Vignali C., Comastri A., Brusa M., Cappelluti N., Iwasawa K., 2014, MNRAS, 445, 3557
Whittam I. H., Green D. A., Jarvis M. J., Riley J. M., 2017, MNRAS, 464, 3357
Williams W. L. et al., 2016, MNRAS, 460, 2385
Wilman R. J. et al., 2008, MNRAS, 388, 1335
Windhorst R., Mathis D., Neuschaefer L., 1990, in Kron R. G., ed., ASP Conf. Ser. Vol. 10, Evolution of the Universe of Galaxies. Astron. Soc. Pac., San Francisco, p. 389
Windhorst R. A., 1984, PhD thesis, Univ. Leiden
Windhorst R. A. et al., 2011, ApJS, 193, 27
Zwart J. et al., 2015, Proc. Sci., Astronomy Below the Survey Threshold in the SKA Era. SISSA, Trieste, PoS(AASKA14)172

APPENDIX: POSTAGE STAMPS

Postage stamps of extended sources, including those merged into single sources, are shown in Fig. A1.

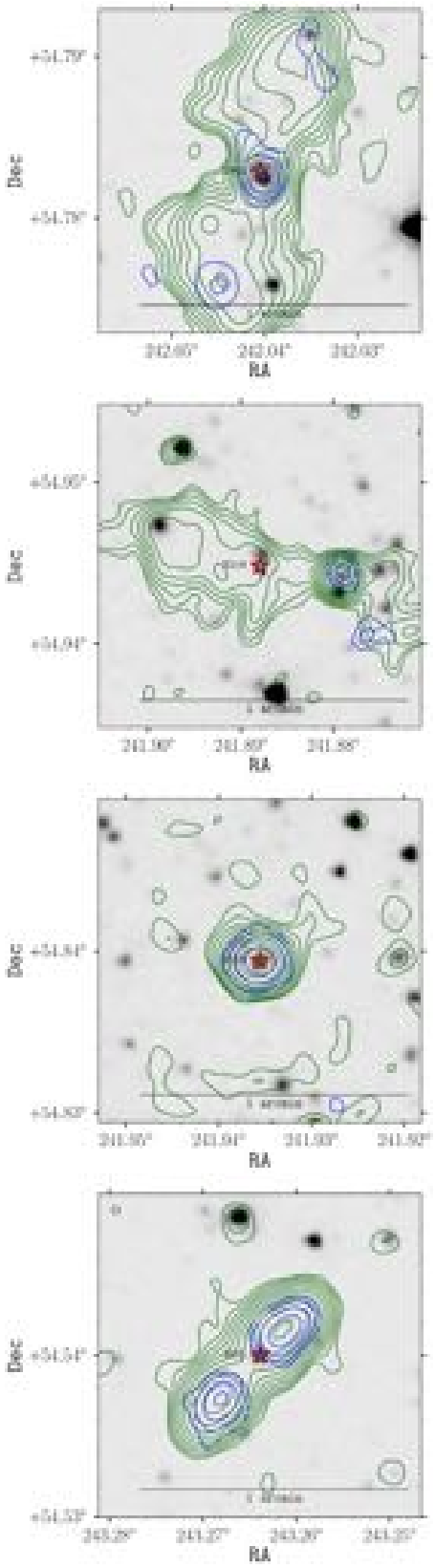

Figure A1. Postage stamps showing examples of extended sources in the GMRT 610 MHz catalogue. The greyscale shows IRAC band 1 images. The green contours represents the GMRT 610 MHz, whereas the blue contours represents VLA FIRST.

This paper has been typeset from a TEX/LATEX file prepared by the author.